Quasi-1D Modelling of Particle-Laden Internal Turbulent Flows with Nucleation, Agglomeration and Breakup

Application to Asphaltenes Deposition in Oil Wells

Author: **Mohsen Moghadasi Barazandeh**

Student No.: **4736230**

Supervisor: **Dr. Luis Portela**

Defence Committee Members:

Dr. Luis Portela

Dr. William Rossen

Dr. Pacelli Zitha

Defence Date:

29 Aug 2019

Department of Civil Engineering and Geosciences
Delft University of Technology
The Netherlands

Abstract

Particle-laden internal turbulent flows are very commonplace, for example, in petrochemical flowlines, oil wells and so on. From an engineering view point, modelling such flows in a 3D or even 2D fashion may not be reasonable in terms of computational cost, especially when the flow domain is sufficiently long, and a large number of grid cells are needed to resolve the flow field. On the other hand, 1D models are quite fast but only take into account the stream-wise variations of the flow characteristics, without providing any information on their cross-sectional distribution. In this work, a novel quasi-1D modelling framework was introduced, which is able to capture the flow field in both stream-wise and cross-stream directions and yet stay computationally more efficient than the 3D or 2D models.

The quasi-1D modelling framework was developed based on the one-way coupling of a RANS model for the single-phase turbulent flow with an Eulerian model for the transport of the dispersed particle phase. The nucleation, agglomeration and breakup events were also taken into consideration through the generic population balance equation, the solution of which was provided using the direct quadrature method of moments.

The results of the quasi-1D single-phase flow model were verified and shown to be in accordance with those of the ANSYS Fluent 2D model for different test cases. The computational cost analysis revealed that the simulation CPU time of the quasi-1D model increases linearly with the number of stream-wise grid cells (N_x), whereas that of the 2D model scales with $N_x^{1.6}$, implying that the quasi-1D model will perform faster than the 2D model from a certain number of grid cells on.

The quasi-1D multi-phase-flow tool was then used to address the transport and deposition of asphaltenes in oil wells, as an example of particle-laden internal turbulent flows. To this end, a simulation test case was set up with several simplifications, and the results were compared with those of a simpler 1D model in the literature, as the benchmark. Due to the lack of an appropriate model for the collision efficiency of asphaltene particles, a model associated with liquid droplets was adopted and tuned to obtain a match between the results of this study and the benchmark. The outcome of the sensitivity analysis demonstrated that the collision efficiency plays an important role in determining the asphaltene deposition profile along the well bore and needs to be modeled accurately.

Table of Contents

Introduction

Particle-laden internal turbulent flows are of high importance in a variety of natural and engineering applications. Transport of slurries in pipes, species in petrochemichal flowlines and hydrocarbon precipitants in oil wells are among the imaginable examples. Such flows have been studied for decades using various experimental and computational techniques. However, there is still room to conduct more investigations and contribute to the knowledge in this filed.

One of the several methods for modelling the particle-laden turbulent flows is referred to as the Eulerian-Eulerian or two-fluid approach, which considers the carrier fluid as the continuous phase and the particles as the dispersed phase. The conservation of mass and momentum are formulated for each phase through ensemble averaging and may involve different levels of complexity, arising from the particle-fluid and particle-particle interactions (see e.g. Schwarzkopf et al., 2011).

Depending on the physical nature of the flow, the corresponding conservation equations may be applied in 3D, 2D and 1D modes. On the one hand, when the flow domain is very long and a large number of grid cells are required to resolve the flow field in the stream-wise direction, the implementation of 3D and 2D models would be computationally expensive. On the other hand, even though a 1D model can be very fast, it only takes into account the stream-wise variation of the flow characteristics and provides no information on their distribution over the cross section. A novel quasi-1D modelling approach will be developed in this work, which not only captures the flow field in both the stream-wise and cross-stream directions, but also stays computationally more efficient than a 2D model.

The basic idea of the quasi-1D approach is to split the 2D conservation equations into 1D equations over the stream-wise and cross-stream directions and solve them in an interative manner, which will allow to achieve a less computational cost, compared with a 2D model, and yet be able resolve the flow field in both directions, as apposed to a 1D model. For the sake of simplicity, the quasi-1D modelling concept and the corresponding equations will be presented for a channel geometry. However, it should be noted that a similar procedure can be followed to derive the equations for a pipe geometry as well.

In this work, the one-way coupling assumption will be made, base on which only the carrier fluid influences the particles movement, and the inter-particle forces are also neglected. A RANS model will be employed to describe the turbulent flow of the continuous phase, and an Eulerian model will be used to account for the particles transport. Moreover, the nucleation, agglomeration and breakup of the particles will be taken into consideration through the population balance equation, which will be solved using the direct quadrature method of moments.

An application of the quasi-1D multi-phase-flow tool is in modelling the transport and deposition of asphaltenes in oil wells. The crude oil is composed of a broad diversity of components, ranging from very light to very heavy. Asphaltenes are the most polar and aromatic fraction of the crude oil heavy components (Schutte, 2016). Depending on the pressure and temperature conditions, the asphaltenes may precipitate out of the crude oil in the form of either liquid drops or solid particles, which are totally referred to as asphaltene particles in this work.

The crude oil is produced from a reservoir in the subsurface and flows through a vertical well up to the surface. The pressure and temperature variations along the well bore may trigger the

asphaltenes to precipitate. The precipitated particles will be transported along with the flow in both stream-wise and cross-stream directions and will undergo various processes such as agglomeration and breakage. They can also deposit on the walls of the well bore and reduce its diameter, which will cause higher pressure drop and restrict the flow rate.

Numerous approaches have been developed so far to address the deposition of asphaltenes in oil wells, which can be classified into two major groups. In the first group of approaches, empirical multi-phase-flow models are employed to obtain the pressure and temperature distributions along the well bore, based on which the concentration of precipitated asphaltenes is calculated using a thermodynamic equation of state (EOS). Then, the in-situ deposition flux is attained from an empirical expression, which may involve various deposition mechanisms such as Brownian diffusion, turbulent diffusion etc., without taking into account the processes associated with the particles transport (Ramirez-Jaramillo et al., 2006, Kor; R. Kharrat, 2016). The second group of methods couple a thermodynamic EOS with a one-dimensional transport equation for the concentration of asphaltenes. The EOS describes the precipitation rate as a function of the pressure and temperature variations, which then serves as input to the transport equation to determine how the particles will move along with the flow and deposit on the walls of the domain. The depletion of mass due to the deposition is also taken into account via a source term in the transport equation (Vargas et al., 2010 and Kurup et al., 2011).

A one-dimensional transport equation only takes into account an average concentration over each cross section. However, if the concentration highly varies in the cross-stream direction, the average of the corresponding profile will be completely different from the concentration at the position of the wall, which determines the deposition flux (Fig. 1). This might lead to an unreliable prediction of the deposition profile along the well bore.

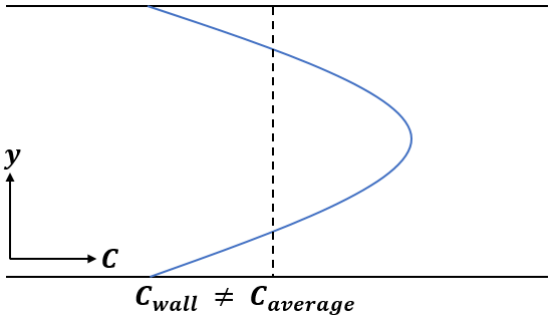

Fig. 1: Cross-sectional asphaltene concentration profile

The above-mentioned issue will be addressed in this work using the quasi-1D modelling approach, which can resolve the profile of the concentration over each cross section and accurately determine the respective value at the wall.

Outline

In chapter 1, the basic idea of the quasi-1D approach will be elaborated on for a single-phase turbulent channel flow using a RANS model. The quasi-1D form of the conservation equations will be derived from the corresponding 2D equations, and the solution procedures will be discussed. The simulation results will be presented for different test cases and verified against those of the ANSYS Fluent 2D model.

In chapter 2, an Eulerian model will be employed to describe the transport of particles based on the one-way coupling assumption, and the generic population balance equation will be incorporated to take into account the nucleation, agglomeration and breakup events. The application of the direct quadrature method of moments (DQMOM) in solving the population balance equation will be explained. Following a similar procedure as in chapter 1, the quasi-1D form of the particle transport equations will be derived and the respective solution algorithms will be provided.

In chapter 3, the quasi-1D multi-phase-flow tool will be used in to address the transport and deposition of asphaltenes in oil wells, as an example of particle-laden internal turbulent flows. A simulation test case will be set up according to the work of Kurup et al., 2011, who used a simpler 1D model, and the corresponding results will be compared.

Chapter 1

Fluid Flow Modeling

This chapter is dedicated to steady state modeling of single-phase turbulent fluid flow in a channel within the quasi-1D framework. In the first place, the theory and applicability of the quasi-1D condition will be elaborated on. Then, the respective governing conservation equations will be presented in both differential and discretized forms, followed by the corresponding algorithms used to solve this set of equations. The reliability of the model will be investigated for different test cases by validating its results with those of the academic version of Ansys Fluent 2019.

1.1 Philosophy of Quasi-1D Assumption

In many fluid dynamical processes such as flow in pipelines, channels, rivers etc., the change of flow properties in one direction is much more rapid than in the other directions. Therefore, from an engineering point of view, it might be sufficient to pay more attention to the direction where a greater level of variations is occurring rather than trying to resolve the physics involved in all the directions. This is where the quasi-1D idea comes into play, which can lead to satisfactorily accurate results with less computational effort, when compared with 3D or 2D simulations.

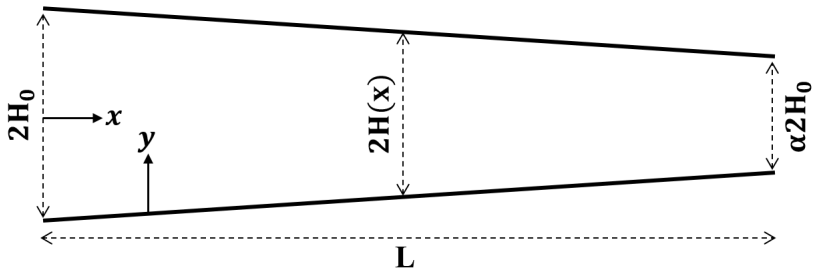

Fig. 1.1: Quasi-1D channel geometry

In order to comprehend the quasi-1D concept clearly, consider a channel geometry whose width is gradually decreasing in the stream-wise direction (Fig. 1.1), which is essentially the same as a pipeline with gradually reducing diameter. Note that the x coordinate, starting from the inlet, points towards the stream-wise direction, and the y coordinate, with its reference on the bottom wall, points towards the cross-stream direction. For the sake of simplicity, suppose that the flow is laminar and at steady state.

If the channel width did not change along the x-axis, the x-velocity field U would stay uniform in the stream-wise direction based on the fully developed flow condition:

$$\frac{\partial U}{\partial x} = 0$$

However, now that the channel width is incrementally varying, it can be inferred that the velocity will also change very slowly in the x direction. On the other hand, it is well established that the cross-sectional profile of the x-velocity $U(y)$ is of a parabolic shape as illustrated in Fig. 1.2.

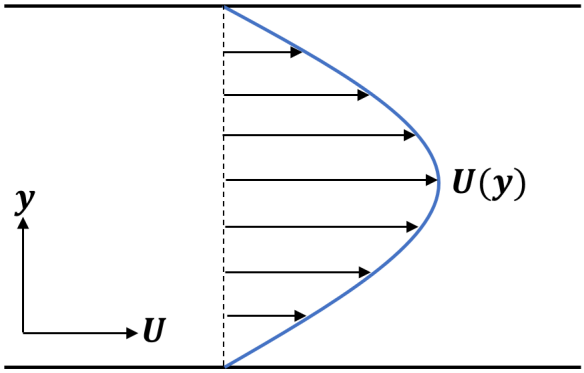

Fig. 1.2: Laminar flow cross-sectional velocity profile

It is clearly seen that the variation of the x-velocity in the cross-stream direction is much more extreme than in the stream-wise direction, or in other words:

$$\frac{\partial U}{\partial y} \gg \frac{\partial U}{\partial x}$$

which implies that the velocity field can be obtained by resolving the cross-sectional profiles of the x-velocity along the channel. To do so, the 2D flow equation is split into a stream-wise 1D equation and a cross-stream 1D equation. The former is used to obtain the distribution of the average x-velocity along the channel, based on which the latter is applied to construct the cross-sectional velocity profiles, providing information again to correct how the average x-velocity will vary stream-wise. This is the basic idea of the quasi-1D approach, which is presumed to achieve more or less the same results as a 2D model but in the hope of less computational cost.

Even though only explained for a simple steady-state laminar flow in a gradually contracting channel, the quasi-1 framework can embed any transport phenomena with variations in one direction dominating over the other directions, a good example of which is the transport and deposition of asphaltene particles in oil wells that will be addressed in chapter 3.

1.2 Quasi-Steady-State Condition

The single-phase flow model, to be developed in this chapter, will later on evolve into a model for particle-laden flows, where the walls of the flow domain are continuously being displaced due to the deposition of particles, which will itself influence the flow characteristics. In case this process occurs very slowly, the flow can be considered to be at a steady state at any given time, and the time derivative terms can be neglected. This is referred to as the quasi-steady-state condition.

1.3 Development of Quasi-1D Methodology

Modeling of any transport phenomena including fluid flow starts with working out the governing conservation equations for the system of interest, which will then be simplified using some reasonable assumptions. The two conservation laws used to describe the incompressible fluid flow are the continuity and Navier-Stokes equations:

$$\frac{\partial U_c}{\partial x} + \frac{\partial V_c}{\partial y} = 0 \tag{1.1}$$

$$\frac{\partial U_c}{\partial t} + \frac{\partial U_c^2}{\partial x} + \frac{\partial (U_c V_c)}{\partial y} = -\frac{1}{\rho}\frac{\partial P_c}{\partial x} + \frac{\partial}{\partial x}\left(\nu \frac{\partial U_c}{\partial x}\right) + \frac{\partial}{\partial y}\left(\nu \frac{\partial U_c}{\partial y}\right) \tag{1.2}$$

where U and V represent the fluid velocity in the stream-wise and cross-stream directions, respectively, each bearing the subscript c standing for "continuous phase". One may decide to achieve the steady state for the flow by solving the corresponding steady equations directly. However, this will lead to convergence problems if the steady-state solution of the equations is too far from the initial guess for the solution. An effective way of resolving this issue is to consider a pseudo time term, as appears in Eqn. (1.2), start from an "artificial" initial condition, and solve the equations until the flow characteristics do not vary in time anymore.

The effect of turbulence is taken into account by introducing the Reynolds averaged form of the Navier-Stokes and continuity equations:

$$\frac{\partial \langle U_c \rangle}{\partial x} + \frac{\partial \langle V_c \rangle}{\partial y} = 0 \tag{1.3}$$

$$\frac{\partial \langle U_c \rangle}{\partial t} + \frac{\partial \langle U_c \rangle^2}{\partial x} + \frac{\partial (\langle U_c \rangle \langle V_c \rangle)}{\partial y} + \frac{\partial \langle U_c'^2 \rangle}{\partial x} + \frac{\partial \langle U_c' V_c' \rangle}{\partial y} = -\frac{1}{\rho}\frac{\partial \langle P_c \rangle}{\partial x} + \frac{\partial}{\partial x}\left(\nu \frac{\partial \langle U_c \rangle}{\partial x}\right) + \frac{\partial}{\partial y}\left(\nu \frac{\partial \langle U_c \rangle}{\partial y}\right) \tag{1.4}$$

that are derived through substituting the Reynolds decomposition of the velocity components and the pressure, defined as:

$$U_c = \langle U_c \rangle + U_c'$$
$$V_c = \langle V_c \rangle + V_c'$$
$$P_c = \langle P_c \rangle + P_c'$$

into Eqn. (1.1) and (1.2), and then applying the ensemble averaging (notated by angle bracket) to the resulting equations. Ignoring the cross-stream mean flow velocity $\langle V_c \rangle$ and also the stream-wise variation of the turbulence, Eqn. (1.3) and (1.4) will be reduced to:

$$\frac{\partial \langle U_c \rangle}{\partial x} = 0 \tag{1.5}$$

$$\frac{\partial \langle U_c \rangle}{\partial t} + \frac{\partial \langle U_c' V_c' \rangle}{\partial y} = -\frac{1}{\rho}\frac{\partial \langle P_c \rangle}{\partial x} + \frac{\partial}{\partial y}\left(\nu \frac{\partial \langle U_c \rangle}{\partial y}\right) \tag{1.6}$$

In order to close the last term (Reynolds Stress Flux) on the right hand side of Eqn. (1.6), the Boussinesq hypothesis is used as follows:

$$-\langle U_c' V_c' \rangle = 2\nu_t \frac{\partial \langle U_c \rangle}{\partial y} \tag{1.7}$$

where ν_t is the turbulent viscosity. Combining this relation with Eqn. (1.6) yields:

$$\frac{\partial \langle U_c \rangle}{\partial t} + \frac{\partial \langle U_c \rangle^2}{\partial x} = -\frac{1}{\rho}\frac{\partial \langle P_c \rangle}{\partial x} + \frac{\partial}{\partial y}\left((\nu + \nu_t)\frac{\partial \langle U_c \rangle}{\partial y}\right) \tag{1.8}$$

which may be rewritten into:

$$\frac{\partial \langle U_c \rangle}{\partial t} + \frac{\partial \langle U_c \rangle^2}{\partial x} = -\frac{1}{\rho}\frac{\partial \langle P_c \rangle}{\partial x} + \frac{\partial \mathcal{T}}{\partial y} \tag{1.9}$$

with $\mathcal{T}$ referring to the total shear stress. This equation along with Eqn. (1.5) constitute the starting point for quasi-1D modelling of the flow. As mentioned in Section 1.1, the basis of the quasi-1D approach is to split the flow equation in the stream-wise and cross-stream directions and, instead of a 2D equation, solve two 1D equations in an iterative manner. To this end, Eqn. (1.5) and (1.9) are integrated with respect to y, from 0 to H:

$$\int_0^H \frac{\partial \langle U_c \rangle}{\partial x} \mathrm{d}y = 0 \tag{1.10}$$

$$\int_0^H \frac{\partial \langle U_c \rangle}{\partial t} \mathrm{d}y + \int_0^H \frac{\partial \langle U_c \rangle^2}{\partial x} \mathrm{d}y = \int_0^H -\frac{1}{\rho}\frac{\partial \langle P_c \rangle}{\partial x} \mathrm{d}y + \int_0^H \frac{\partial \mathcal{T}}{\partial y} \mathrm{d}y \tag{1.11}$$

which can be manipulated into:

$$\frac{\partial}{\partial x}\int_0^H \langle U_c \rangle \mathrm{d}y = 0 \tag{1.12}$$

$$\frac{\partial}{\partial t}\int_0^H \langle U_c \rangle \mathrm{d}y + \frac{\partial}{\partial x}\int_0^H \langle U_c \rangle^2 \mathrm{d}y = -\frac{1}{\rho}\frac{\partial}{\partial x}\int_0^H \langle P_c \rangle \mathrm{d}y + \mathcal{T}_H - \mathcal{T}_0 \tag{1.13}$$

By introducing the cross-sectional average defined for any flow variable $\beta(y)$ as:

$$\bar{\beta} = \frac{1}{H}\int_0^H \beta(y)\mathrm{d}y \quad \Rightarrow \quad \int_0^H \beta(y)\mathrm{d}y = H\bar{\beta} \tag{1.14}$$

one may rewrite Eqn. (1.12) and (1.13) as:

$$\frac{\partial (H\langle \overline{U}_c \rangle)}{\partial x} = 0 \tag{1.15}$$

$$\frac{\partial(H\langle\overline{U}_c\rangle)}{\partial t} + \frac{\partial(H\overline{\langle U_c\rangle^2})}{\partial x} = -\frac{1}{\rho}\frac{\partial(H\langle\overline{P}_c\rangle)}{\partial x} + \tau_H - \tau_0 \tag{1.16}$$

The advection term on the left hand side of Eqn. (1.16) contains the mean squared velocity, which can be converted to the squared mean velocity using the following definition:

$$\overline{\langle U_c\rangle^2} \equiv F\langle\overline{U}_c\rangle^2$$

where F is the so-called averaging separation factor whose value would deviate more from unity as the velocity profile becomes more nonlinear. In addition, the symmetry condition demands that the total shear stress on the center line of the channel (τ_H) should be zero. After making these changes to Eqn. (1.16), it turns out to:

$$\frac{\partial(H\langle\overline{U}_c\rangle)}{\partial t} + \frac{\partial(FH\langle\overline{U}_c\rangle^2)}{\partial x} = -\frac{1}{\rho}\frac{\partial(H\langle\overline{P}_c\rangle)}{\partial x} - \tau_0 \tag{1.17}$$

This equation in conjunction with Eqn. (1.5) constitute the desired set of 1D equations in the stream-wise direction, which will be used to obtain the distribution of the average flow velocity $\langle\overline{U}_c\rangle$ and pressure $\langle\overline{P}_c\rangle$ along the channel for a given stream-wise distribution of the shear-stress at the wall (τ_0).

The next step would be to acquire the cross-sectional profile of the flow velocity at any x-position along the channel. To do so, the terms bearing x derivative in Eqn. (1.8) are lumped into a "source term" Ψ, which is presumed not to be a function of y:

$$\frac{\partial\langle U_c\rangle}{\partial t} = \frac{\partial}{\partial y}\left((\nu + \nu_t)\frac{\partial\langle U_c\rangle}{\partial y}\right) + \Psi \tag{1.18}$$

It is obvious from this equation that any value of Ψ would result in a velocity profile with a unique cross-sectional average (Fig. 1.3). However, the correct profile is the one whose cross-sectional average is equal to the average velocity provided by Eqn. (1.17) at the respective x-position, which implies that different values of Ψ should be tried until the profile of interest is achieved. For this purpose, the false-position method is used in this work to guide the values of Ψ, for which the initial guess can be calculated from:

$$\Psi_{initial} = -\frac{\partial(FH\langle\overline{U}_c\rangle^2)}{\partial x} - \frac{1}{\rho}\frac{\partial(H\langle\overline{P}_c\rangle)}{\partial x} \tag{1.19}$$

Once the velocity profiles are constructed along the channel, the x-distribution of the wall shear-stress, to be re-substituted into Eqn. (1.17), will be updated. Therefore, an iterative procedure can be considered between the stream-wise 1D equations (Eqn. 1.15 and 1.17) and the cross-stream 1D equations (Eqn. 1.8) through the wall shear-stress.

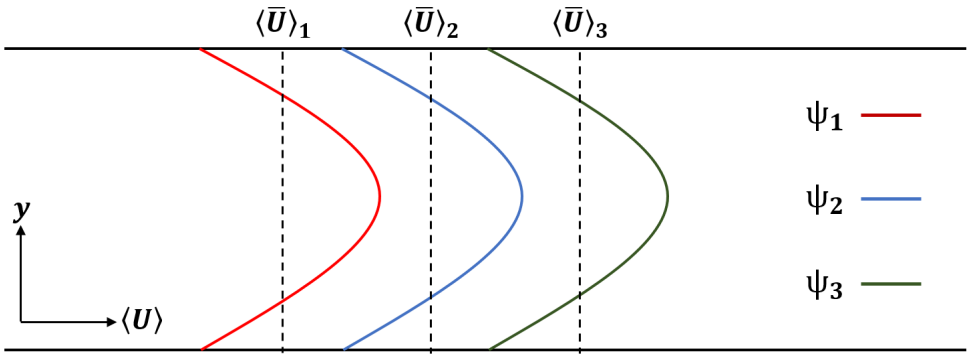

Fig. 1.3: Effect of Ψ on velocity profile

1.3.1 $k-\varepsilon$ Model

In this work, the turbulent viscosity ν_t is supplied by the $k-\varepsilon$ model (see e.g. Schäfer, 2006) as:

$$\nu_t = C_\mu \frac{k^2}{\varepsilon} \tag{1.20}$$

where the turbulent kinetic energy k and its dissipation rate ε are given by their own transport equations whose steady-state forms read:

$$-\frac{\partial}{\partial y}\left[(\nu + \frac{\nu_t}{\sigma_k})\frac{\partial k}{\partial y}\right] = \nu_t\left(\frac{\partial \langle U_c\rangle}{\partial y}\right)^2 - \varepsilon \tag{1.21}$$

$$-\frac{\partial}{\partial y}\left[(\nu + \frac{\nu_t}{\sigma_\varepsilon})\frac{\partial \varepsilon}{\partial y}\right] = C_{\varepsilon 1}\nu_t\left(\frac{\partial \langle U_c\rangle}{\partial y}\right)^2\frac{\varepsilon}{k} - C_{\varepsilon 2}\frac{\varepsilon^2}{k} \tag{1.22}$$

The constants C_μ, $C_{\varepsilon 1}$ and $C_{\varepsilon 2}$ are taken equal to 0.09, 1.44 and 1.92, respectively, which are the standard values.

1.3.2 Standard Wall Function with Roughness

The dimensionless mean velocity and wall distance are introduced as:

$$u^+ = \frac{\langle U_c\rangle}{u_*} \quad \& \quad y^+ = \frac{y u_*}{\nu}$$

where u_* is called the friction velocity and defined as:

$$u_* = \sqrt{\frac{\tau_0}{\rho}}$$

Fig. 1.4 illustrates the universal behavior of the dimensionless mean flow velocity near a smooth wall with various distinguishable regions (Tab. 1.1). In the logarithmic region, the following relation exists between the mean velocity and the the distance from the wall:

$$\frac{\langle U_c \rangle_L}{u_*} = \frac{1}{\kappa} \ln\left(\frac{y_L u_*}{\nu}\right) + 4.88 \tag{1.23}$$

in which κ is Von Karman constant, taken roughly equal to 0.41, and subscript L refers to the logarithmic layer.

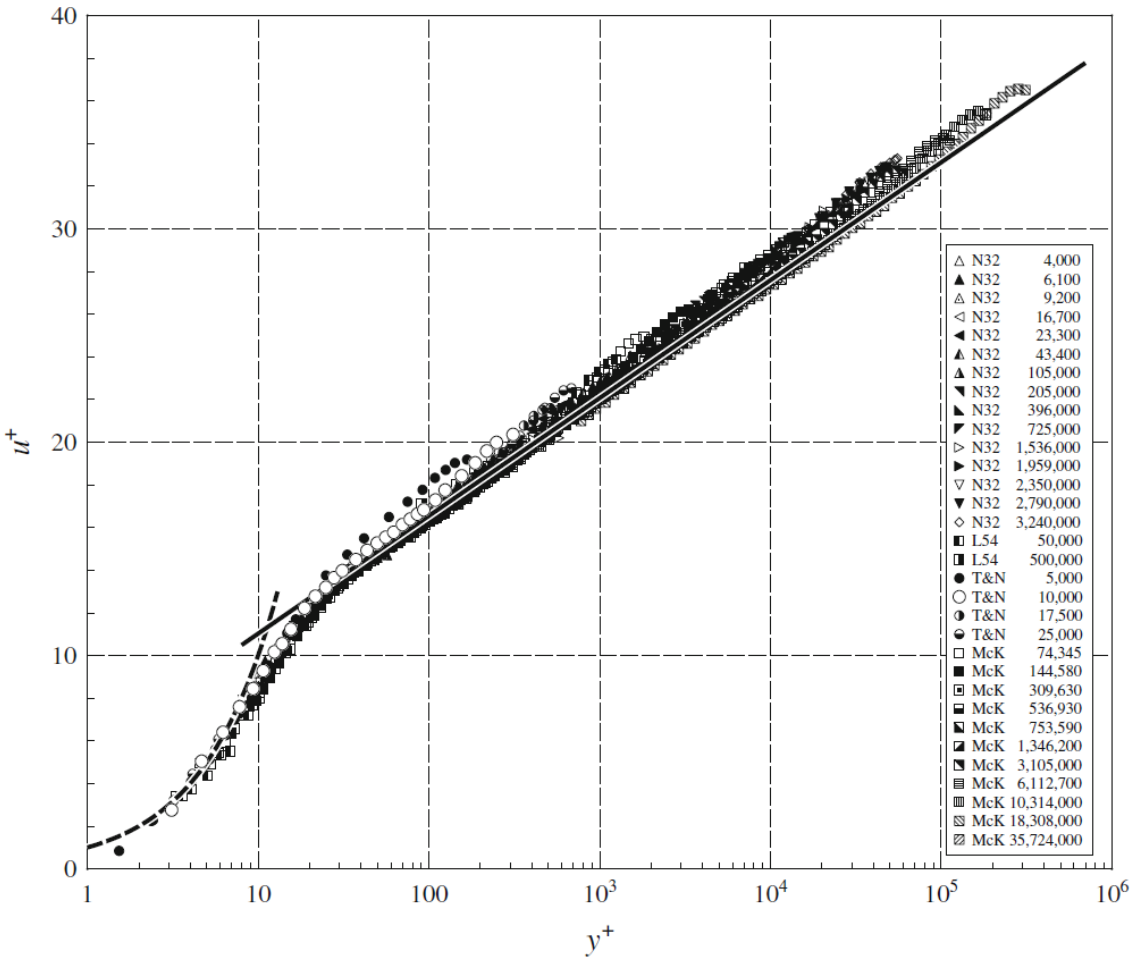

Fig. 1.4: Dimensionless mean velocity profile as a function of dimensionless wall distance for a turbulent pipe flow with Reynolds numbers between 4×10^3 and 36×10^6 (Nieuwstadt et al., 2016)

Viscous Sublayer	Buffer Layer	Logarithmic Layer
$y^+ \leq 5$	$5 < y^+ < 30$	$30 \leq y^+ \leq 0.22H^+$

Table 1.1: Near-Wall Flow Regions

Eqn. (1.23) is called the standard wall function for smooth walls and can be used as the boundary condition to Eqn. (1.18) in numerical simulations. Application of the wall function in fact has the advantage of skipping the need for an unacceptably large number of grid cells to resolve all the near-wall flow layers since it directly relates the mean velocity in the logarithmic layer to the shear-stress at the wall. This requires the size of the grid cell adjacent to the wall to be set such that the cell center falls into the logarithmic range (Fig. 1.5).

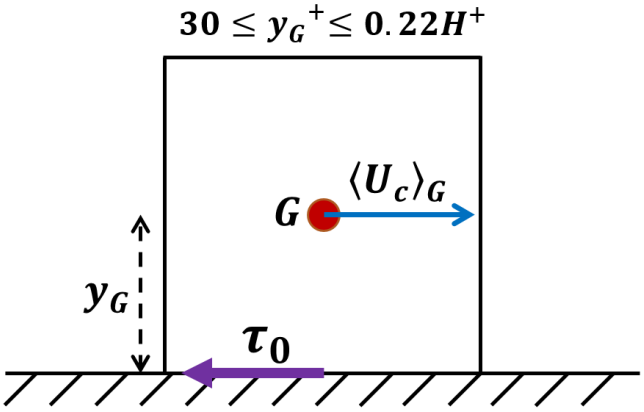

Fig. 1.5: Wall function grid cell

In most particle-laden flows, Eqn. (1.23) is not applicable since the wall surface does not remain smooth anymore, due to the particles deposition. Apsley, 2007 developed a wall function to cope with arbitrarily rough surfaces, with the ability to reproduce the Darcy friction factor, as follows:

$$\frac{\langle U_c \rangle_L}{u_*} = \frac{1}{\kappa} \ln\left(\frac{y_G u_*}{\nu}\right) + B \tag{1.24}$$

with:

$$B = 8 - \frac{1}{\kappa} \ln\left(\frac{k_s u_*}{\nu} + 3.152\right)$$

where k_s represents the absolute roughness. In addition, assuming that the production and dissipation of the turbulent kinetic energy are in equilibrium within the logarithmic layer, the values of the turbulent kinetic energy and its dissipation rate can be estimated at y_G, to be utilized as the boundary condition to Eqn. (1.21) and Eqn. (1.22), respectively:

$$k_L = \frac{u_*^2}{\sqrt{C_\mu}} \tag{1.25}$$

$$\varepsilon_L = \frac{u_*^3}{\kappa(y_L - y_d)} \tag{1.26}$$

where:

$$y_d^+ = \begin{cases} B - \frac{1}{\kappa}(\ln \kappa + 1) & B - \frac{1}{\kappa} \ln \kappa \geq 0 \\ -\frac{1}{\kappa} e^{-\kappa(B - \frac{1}{\kappa} \ln \kappa)} & B - \frac{1}{\kappa} \ln \kappa \leq 0 \end{cases}$$

1.3.3 Iteration Procedure

As mentioned before, the solution of the single-phase flow model within the quasi-1D framework is achieved through iterating between the stream-wise and cross-stream 1D equations, which has been schematically depicted below:

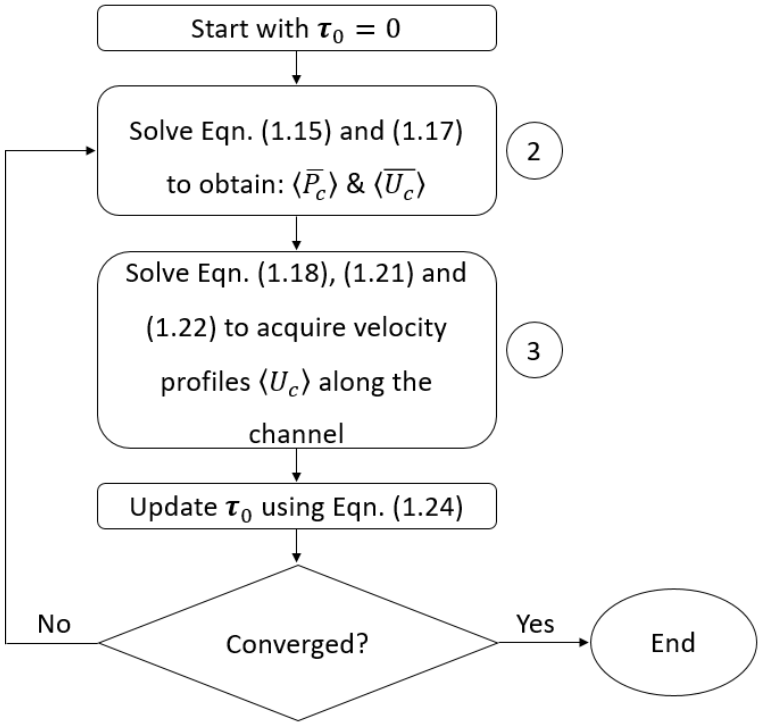

Fig. 1.6: Iteration procedure for single-phase flow

Each of the steps 2 and 3 includes inner iteration, which will be expanded on in the subsequent section.

1.4 Numerical Solution for Flow Equations

Since no analytical solution exists for the flow equations derived in the former section, the numerical approaches such as finite difference, finite volume and so on come into play, the basis of which is to discretize the differential equations on the domain of interest that is already meshed and solve the resulting set of algebraic equations, written in the matrix form as follows, simultaneously:

$$AX = B \tag{1.27}$$

where A, X and B are the matrix of coefficients, the vector of unknowns and the vector of knowns, respectively. Since all the differential equations to be discretized in the quasi-1D framework are 1D, the resulting A matrix will turn out to be tridiagonal, so that the very efficient Thomas algorithm (see Appendix) can be used to solve Eqn. (1.27).

In this study, the spatial derivatives are approximated using the central differencing scheme, essentially because it is second-order accurate and also leads to a tri-diagonal configuration for the

above-mentioned matrix A, which is not the case when applying higher-order methods. Besides, the time derivative is discretized by the Eulerian first-order backward differencing scheme whose implicit nature helps to circumvent the instability issues associated with the time step size Δt selection. However, this does not necessarily mean that Δt can be set as large as possible since it might destroy the connectivity between the equations under iteration. Note that using higher-order methods for approximating the time derivative is unnecessary regarding the fact that the final goal here is to reach a steady state, at which the flow characteristics are independent of time.

1.4.1 Stream-Wise 1D Equations (SIMPLE Algorithm)

The two unknowns that are going to be determined here are the average velocity and pressure along the channel, for a given stream-wise distribution of the wall shear-stress. The discretization of Eqn. (1.15) and (1.17) is accomplished on an equidistant staggered grid, where the velocities are placed on the cell interfaces and the pressures occur at the cell centers (Fig. 1.7).

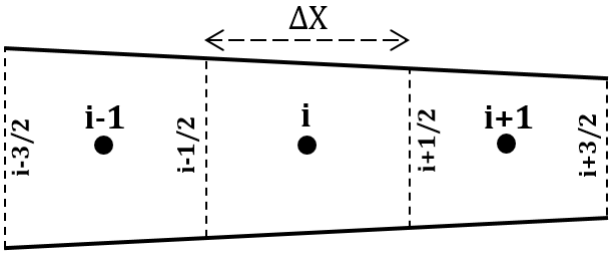

Fig. 1.7: Stream-wise grid stencil

The SIMPLE algorithm (see e.g. Anderson et al., 1995) is used to generate coupling between the pressure and the velocity, which helps to avoid the well known checkerboard pattern in the pressure distribution. In this algorithm, the velocity and pressure at the current time level $n+1$ are written as:

$$\langle \overline{U}_c \rangle^{n+1} = \langle \overline{U}_c \rangle^{*} + \langle \overline{U}_c \rangle'$$
$$\langle \overline{P}_c \rangle^{n+1} = \langle \overline{P}_c \rangle^{*} + \langle \overline{P}_c \rangle'$$

The superscript $*$ denotes the guessed quantity that will be iterated until converging to the actual value, and the term with prime is the residual. The discretized version of Eqn. (1.17) for $\langle \overline{U}_c \rangle^{*}$ on the cell interface $i{+}\frac{1}{2}$ assumes the following form:

$$A_{i-\frac{1}{2}} \langle \overline{U}_c \rangle^{*}_{i-\frac{1}{2}} + A_{i+\frac{1}{2}} \langle \overline{U}_c \rangle^{*}_{i+\frac{1}{2}} + A_{i+\frac{3}{2}} \langle \overline{U}_c \rangle^{*}_{i+\frac{3}{2}} = B_{i+\frac{1}{2}} \tag{1.28}$$

where:

$$A_{i-\frac{1}{2}} = -\frac{H_i\left(\langle\overline{U}_c\rangle^*_{i-\frac{1}{2}} + \langle\overline{U}_c\rangle^*_{i+\frac{1}{2}}\right)}{4\Delta x}$$

$$A_{i+\frac{1}{2}} = \frac{H_{i+\frac{1}{2}}}{\Delta t} - \frac{H_i\left(\langle\overline{U}_c\rangle^*_{i-\frac{1}{2}} + \langle\overline{U}_c\rangle^*_{i+\frac{1}{2}}\right)}{4\Delta x} + \frac{H_{i+1}\left(\langle\overline{U}_c\rangle^*_{i+\frac{1}{2}} + \langle\overline{U}_c\rangle^*_{i+\frac{3}{2}}\right)}{4\Delta x}$$

$$A_{i+\frac{3}{2}} = \frac{H_{i+1}\left(\langle\overline{U}_c\rangle^*_{i+\frac{1}{2}} + \langle\overline{U}_c\rangle^*_{i+\frac{3}{2}}\right)}{4\Delta x}$$

$$B_{i+\frac{1}{2}} = \frac{H_{i+\frac{1}{2}}}{\Delta t}\langle\overline{U}_c\rangle^n_{i+\frac{1}{2}} - \left(\frac{H_{i+\frac{1}{2}}}{\rho\Delta x} + \frac{\Delta H}{2\rho}\right)\langle\overline{P}_c\rangle^*_{i+1} + \left(\frac{H_{i+\frac{1}{2}}}{\rho\Delta x} - \frac{\Delta H}{2\rho}\right)\langle\overline{P}_c\rangle^*_i - \mathcal{T}_{0i+\frac{1}{2}}$$

Note that the velocity also appears in the coefficients of this equation, which results from the linearization of the nonlinear advection term. This requires the velocity to be obtained in an iterative fashion.

The residual pressure at the grid point i is also connected to its counterparts at i−1 and i+1 via the Poisson equation:

$$\begin{aligned} -\left(\frac{H_{i-\frac{1}{2}}}{\Delta x} - \frac{\Delta H_{i-\frac{1}{2}}}{2}\right)\langle\overline{P}_c\rangle'_{i-1} + \left[\left(\frac{H_{i-\frac{1}{2}}}{\Delta x} + \frac{\Delta H_{i-\frac{1}{2}}}{2}\right) + \left(\frac{H_{i+\frac{1}{2}}}{\Delta x} - \frac{\Delta H_{i+\frac{1}{2}}}{2}\right)\right]\langle\overline{P}_c\rangle'_i \\ -\left(\frac{H_{i+\frac{1}{2}}}{\Delta x} + \frac{\Delta H_{i+\frac{1}{2}}}{2}\right)\langle\overline{P}_c\rangle'_{i+1} = \frac{\rho}{\Delta t}\left(H_{i-\frac{1}{2}}\langle\overline{U}_c\rangle^*_{i-\frac{1}{2}} - H_{i+\frac{1}{2}}\langle\overline{U}_c\rangle^*_{i+\frac{1}{2}}\right) \end{aligned} \tag{1.29}$$

which is known as the corrector step in the SIMPLE algorithm. Note that the terms with ΔH account for the extra pressure pushing against the fluid element due to its oblique top and bottom surfaces (Fig. 1.8).

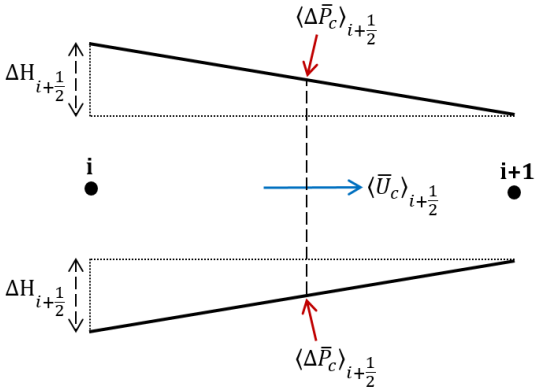

Fig. 1.8: Extra pressure forcing against the fluid element

The way Eqn. (1.28) and (1.29) should be iterated to achieve a convergent solution within a single time step is illustrated in Fig. 1.9.

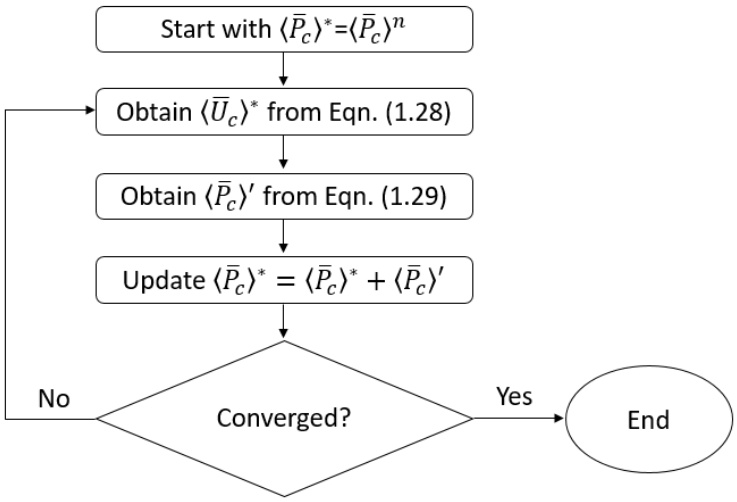

Fig. 1.9: SIMPLE algorithm iteration procedure

The initial guess for $\langle \overline{P}_c \rangle^*$ can be adopted from the pressure distribution in the previous time step.

1.4.2 Cross-Stream 1D Equations

The grid stencil on which the cross-stream 1D equations will be discretized is shown in the figure below:

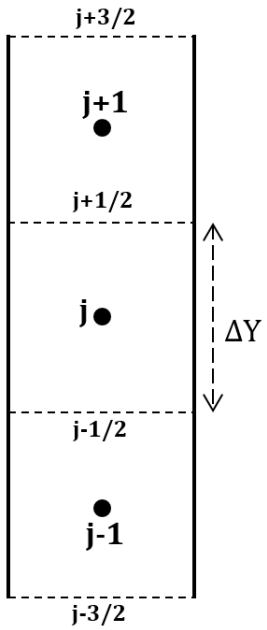

Fig. 1.10: Cross-stream grid stencil

The following are the discrete forms of Eqn. (1.8), (1.21) and (1.22), respectively:

$$-\left[\frac{(\nu_t+\nu)}{\Delta y}\right]_{j-\frac{1}{2}}\langle U_c\rangle_{j-1}^{n+1}+\left\{\frac{1}{\Delta t}+\left[\frac{(\nu_t+\nu)}{\Delta y}\right]_{j-\frac{1}{2}}+\left[\frac{(\nu_t+\nu)}{\Delta y}\right]_{j+\frac{1}{2}}\right\}\langle U_c\rangle_j^{n+1}$$
$$+\left[\frac{(\nu_t+\nu)}{\Delta y}\right]_{j+\frac{1}{2}}\langle U_c\rangle_{j+1}^{n+1}=\frac{\langle U_c\rangle_j^n}{\Delta t}+\Psi\Delta y_j \tag{1.30}$$

$$-\left[\frac{(\nu+\frac{\nu_t}{\sigma_k})}{\Delta y}\right]_{j-\frac{1}{2}}k_{j-1}+\left\{\left[\frac{(\nu+\frac{\nu_t}{\sigma_k})}{\Delta y}\right]_{j-\frac{1}{2}}+\left[\frac{(\nu+\frac{\nu_t}{\sigma_k})}{\Delta y}\right]_{j+\frac{1}{2}}+\left(\frac{\varepsilon}{k}\Delta y\right)_j\right\}k_j$$
$$-\left[\frac{(\nu+\frac{\nu_t}{\sigma_k})}{\Delta y}\right]_{j+\frac{1}{2}}k_{j+1}=\left(\frac{\nu_t}{\Delta t}\right)_j\left(\langle U_c\rangle_{j+\frac{1}{2}}^{n+1}-\langle U_c\rangle_{j-\frac{1}{2}}^{n+1}\right) \tag{1.31}$$

$$-\left[\frac{(\nu+\frac{\nu_t}{\sigma_\varepsilon})}{\Delta y}\right]_{j-\frac{1}{2}}\varepsilon_{j-1}+\left\{\left[\frac{(\nu+\frac{\nu_t}{\sigma_\varepsilon})}{\Delta y}\right]_{j-\frac{1}{2}}+\left[\frac{(\nu+\frac{\nu_t}{\sigma_\varepsilon})}{\Delta y}\right]_{j+\frac{1}{2}}+\left(C_{\varepsilon 2}\frac{\varepsilon}{k}\Delta y\right)_j\right\}\varepsilon_j$$
$$-\left[\frac{(\nu+\frac{\nu_t}{\sigma_\varepsilon})}{\Delta y}\right]_{j+\frac{1}{2}}\varepsilon_{j+1}=\left(C_{\varepsilon 1}\frac{\nu_t}{\Delta t}\frac{\varepsilon}{k}\right)_j\left(\langle U_c\rangle_{j+\frac{1}{2}}^{n+1}-\langle U_c\rangle_{j-\frac{1}{2}}^{n+1}\right) \tag{1.32}$$

As mentioned before, these three equations should be solved for all the cross sections along the channel independently. This is done by varying the value of Ψ at each cross section, using the false-position method, to achieve a velocity profile whose average matches the value already provided by Eqn. (1.28) at the corresponding x-position. The flowchart below explains the iteration procedure applied to arrive at a convergent solution to the above-mentioned equations:

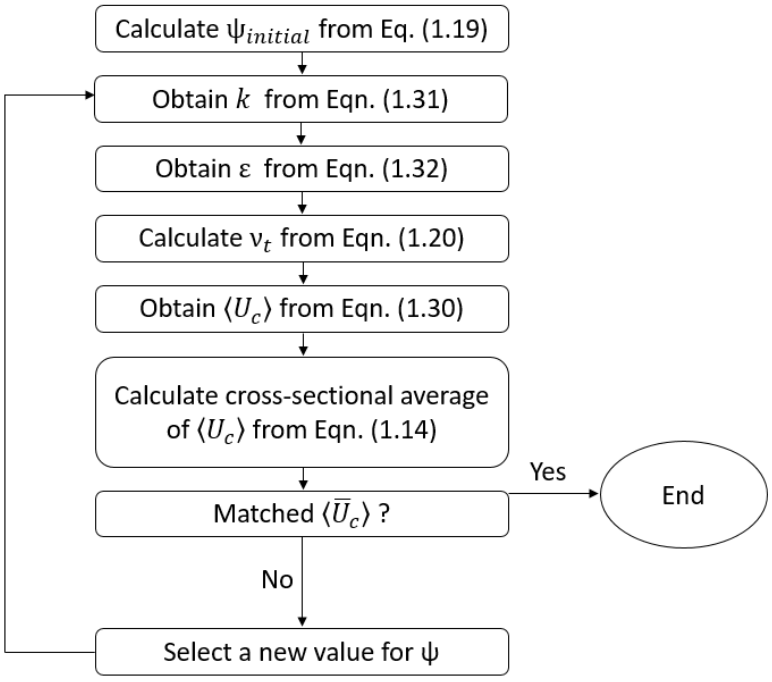

Fig. 1.11: Iteration procedure for cross-stream 1D equations

Note that in each iteration loop, the boundary conditions for $\langle U_c \rangle$, k and ε should be updated using Eqn. (1.24), (1.25) and (1.22), respectively. Moreover, the initial values of these variables, to start the new iteration with, can be adopted from the previous iteration results.

1.4.3 Convergence Criterion

In this study, the following convergence criterion is used to determine whether or not the steady state has been reached:

$$\left| \frac{\xi^{n+1} - \xi^n}{\Delta t} \right| < E$$

where ξ refers to any flow variable such as velocity, and E is an input threshold.

1.5 Results and Discussion

The development of the quasi-1D flow model was thoroughly explained, and the respective equations were worked out. Now, the results of the model will be presented for certain test cases and validated with those of academic ANSYS Fluent 2019 2D model as a benchmark. Fig. 1.12 displays the geometries of the two cases for which the flow simulations were carried out. The first geometry represents a channel whose width linearly decreases down to half of its initial value at the inlet, and the second one depicts a parabolic contraction followed by an expansion. The fluid properties, inlet and outlet boundary conditions, number of stream-wise and cross-stream grid cells (N_x,N_y) and time step size (Δt) have been reported in Tab. 1.2.

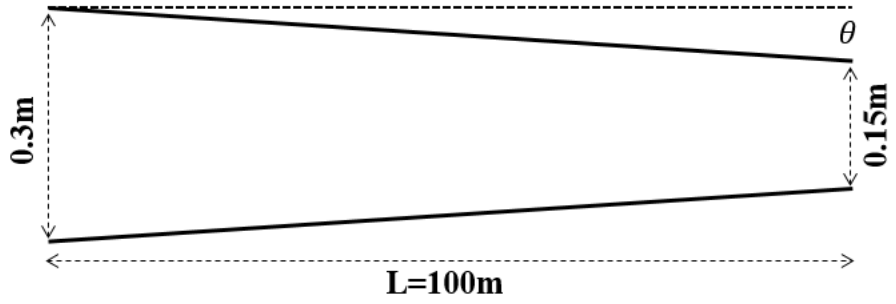

(a) Case1

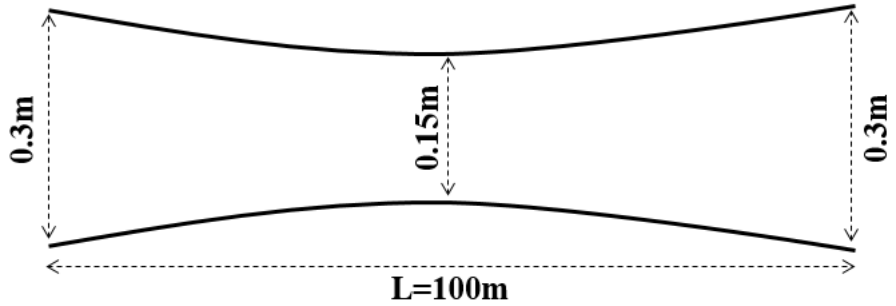

(b) Case2

Fig. 1.12: Geometries of flow simulation test cases

Density $(^{kg}/_{m^3})$	1000
Viscosity $(Pa.s)$	5×10^{-3}
Inlet Velocity $(^{m}/_{s})$	1
Outlet Pressure (Pa)	10^5
N_x & N_y	100 & 30
$\Delta t(s)$	0.2

Table 1.2: Fluid properties and simulation parameters

The velocity and pressure fields of Case1 and Case2 obtained from both the quasi-1D and ANSYS Fluent 2D models are shown in Fig. 1.13 and 1.15, respectively, where the Reynolds. In order to draw a more noticeable comparison, the velocity profiles at the two cross sections $x = 20m$ and $x = 80m$ have also been plotted for both cases (Fig.1.14 and 1.16). It is clearly seen that the results pertaining to the quasi-1D model are in good agreement with those of ANSYS Fluent for both test cases, with a minor discrepancy essentially arising from the fact that the quasi-1D model assumes zero mean flow velocity in the cross-stream direction. As also expected, the pressure field only varies along the channel and is almost uniform within each cross section.

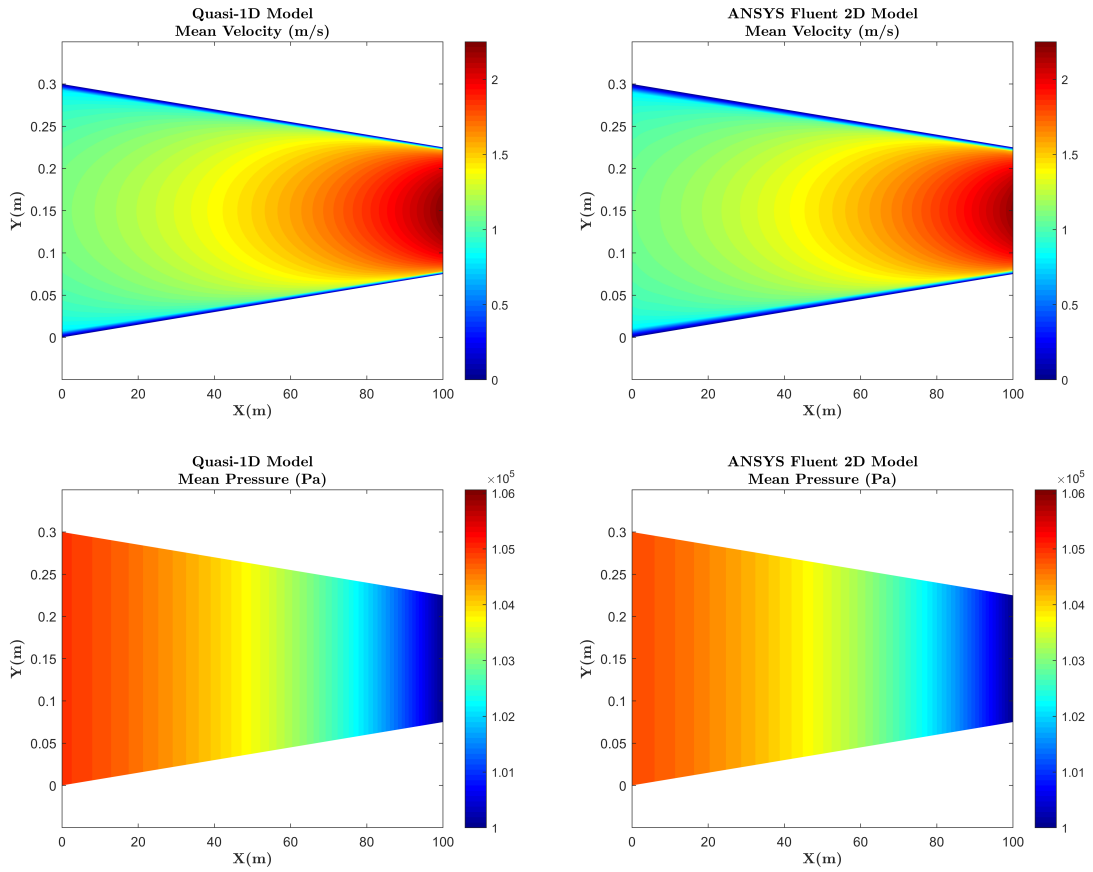

Fig. 1.13: Velocity and pressure fields of Case1 obtained from Quasi-1D model and ANSYS Fluent 2D model

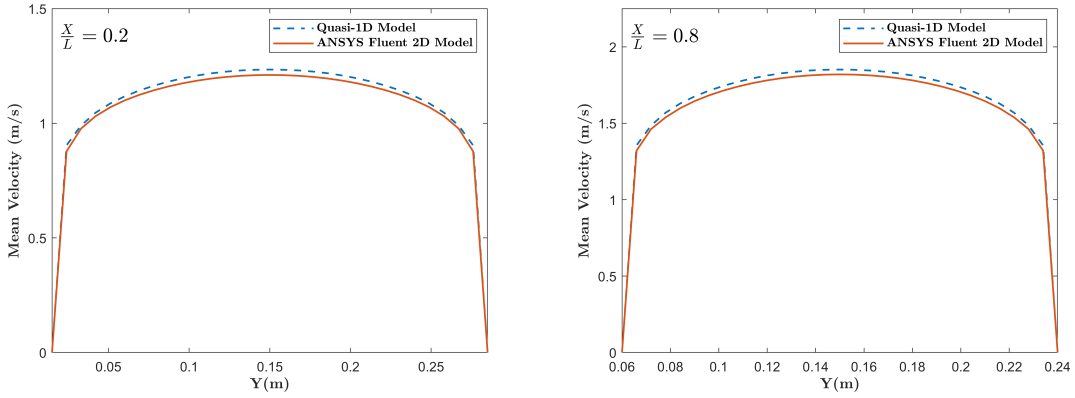

Fig. 1.14: Comparison between velocity profiles of Quasi-1D model and ANSYS Fluent 2D model at cross sections $x = 20m$ and $x = 80m$ for Case1

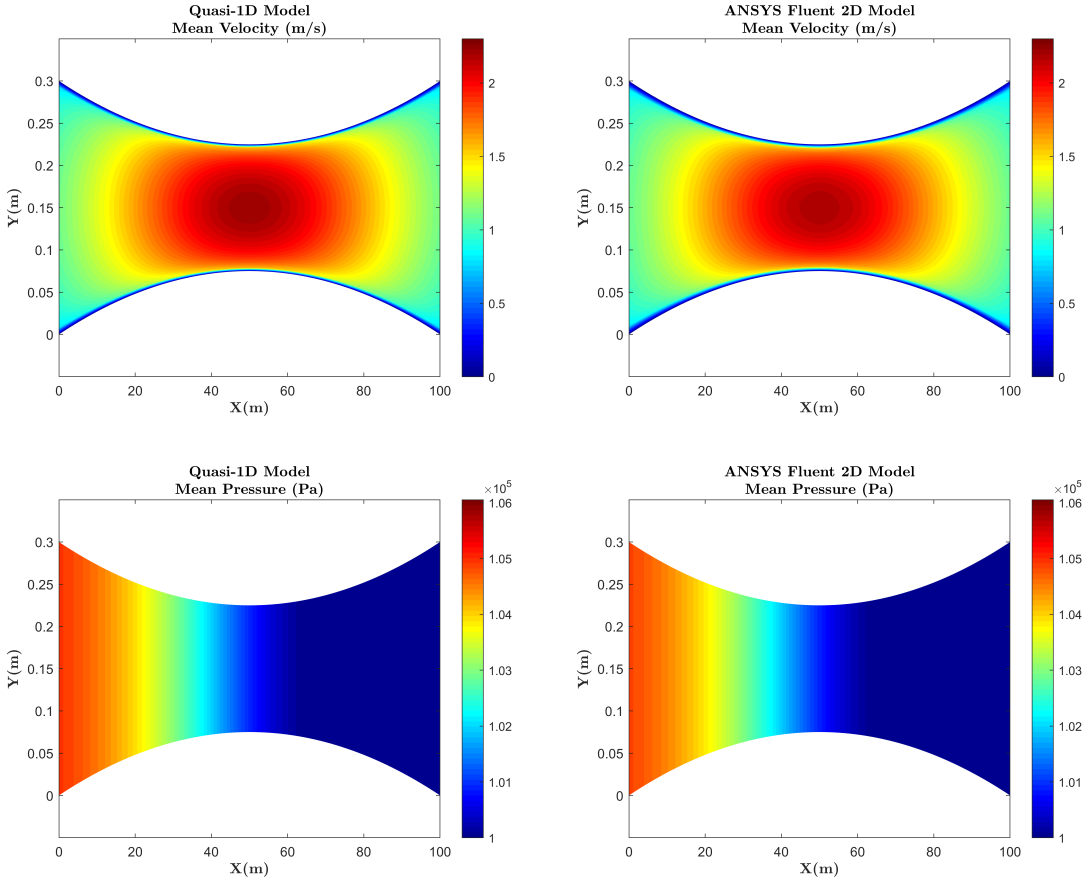

Fig. 1.15: Velocity and pressure fields of Case2 obtained from Quasi-1D model and ANSYS Fluent 2D model

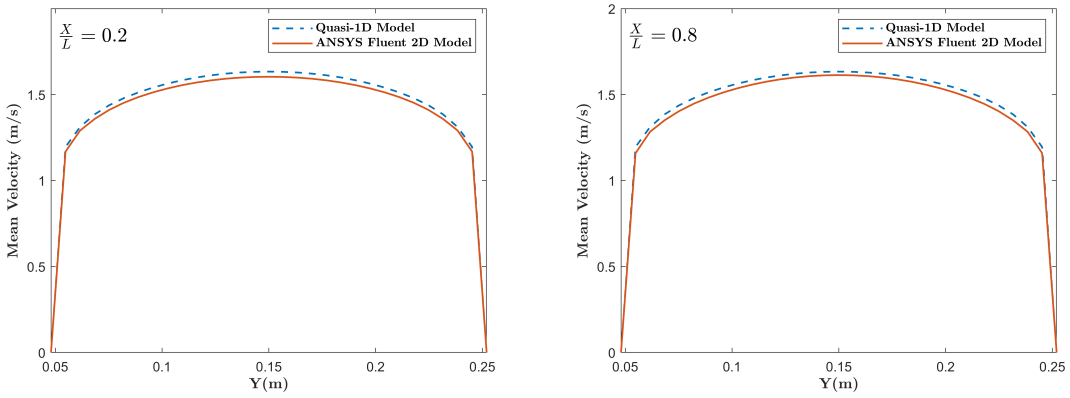

Fig. 1.16: Comparison between velocity profiles of Quasi-1D model and ANSYS Fluent 2D model at cross sections $x = 20m$ and $x = 80m$ for Case2

An interesting subject of curiosity is to investigate to what extent the quasi-1D model stays in accordance with the ANSYS Fluent 2D model. Towards this end, consider the Case1 geometry again, where the contraction angle θ refers to the angle at which the walls of the channel deviate from the horizontal. The aim is to start from $\theta \approx 0$ and increase it by reducing the length of the channel L while keeping the inlet and the outlet width constant in order to see how the mean velocity field of the quasi-1D model changes relative to that of the ANSYS Fluent 2D model. Before doing so, first take a look at Fig. 1.17, which compares the velocity profiles of the two models for $\theta = 0$. In theory, when the geometry is fully 1D, no mean velocity exists in the cross-stream direction, so that the results must be exactly the same. However, a slight discrepancy is still observed, probably due to some differences between the turbulence model parameters used in this study and ANSYS Fluent. This should be taken into account in the rest of the validations.

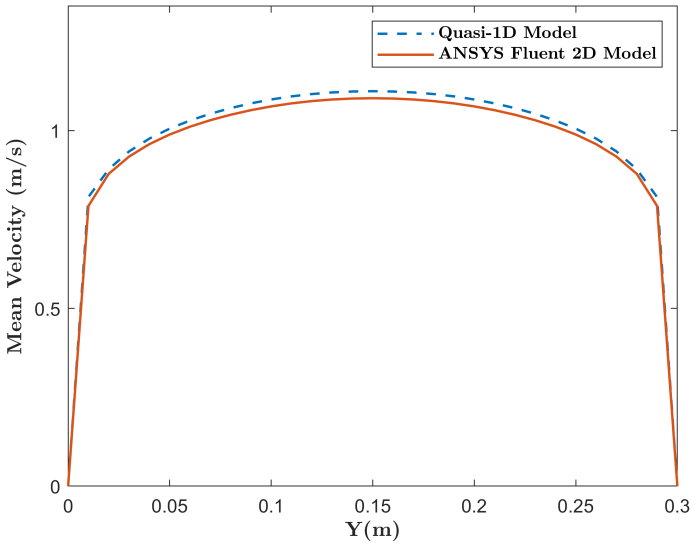

Fig. 1.17: Comparison of mean velocity profiles of Quasi-1D and ANSYS Fluent 2D models for $\theta = 0$

Consider an error parameter defined as:

$$Err = Max\left\{ \left| \frac{\langle U_c \rangle_{Quasi-1D} - \langle U_c \rangle_{ANSYSFluent}}{\langle U_c \rangle_{ANSYSFluent}} \right| \right\} \times 100$$

which is calculated throughout the channel and can be taken as a measure of the departure of the quasi-1D model from the ANSYS Fluent 2D model. Note that the denominator is never close to zero since the minimum velocity within each cross section comes from the logarithmic layer. Fig. 1.18 plots Err as a function of θ, where it is observed that the higher the contraction angle, the larger the error parameter such that as θ is increased above 5°, the agreement between the quasi-1D and ANSYS Fluent 2D models gets more and more degraded. This has also been demonstrated in Fig. 1.19, where the velocity profiles of the two models have been compared for increasing θ at the stream-wise dimensionless position $\frac{x}{L} = 0.2$. However, one may still conclude that the quasi-1D model can be perfectly applied to practical problems such as the deposition of asphaltene in oil wells, to be addressed in chapter 3, where the deposit layer thickness varies gradually in the stream-wise direction.

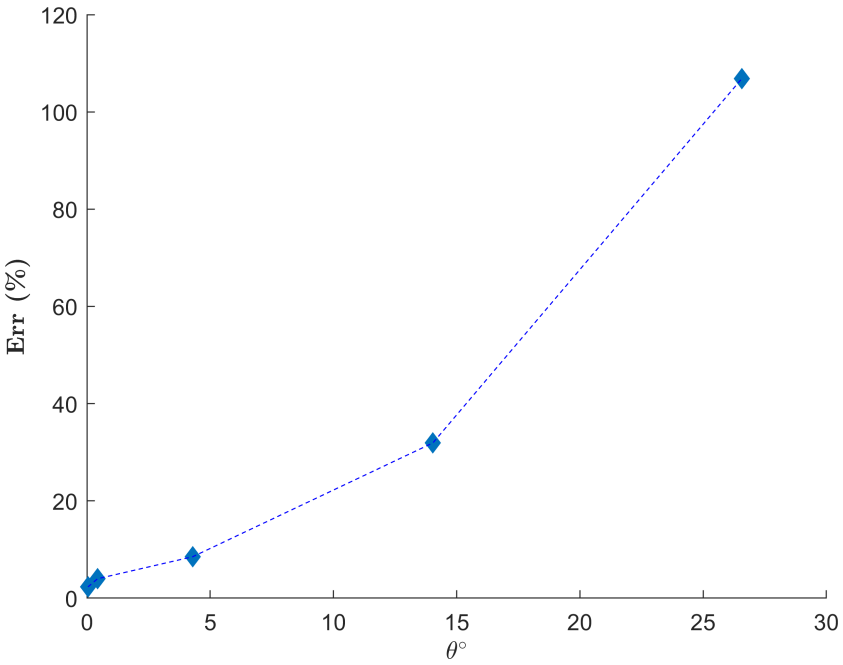

Fig. 1.18: Error parameter as a function of contraction angle

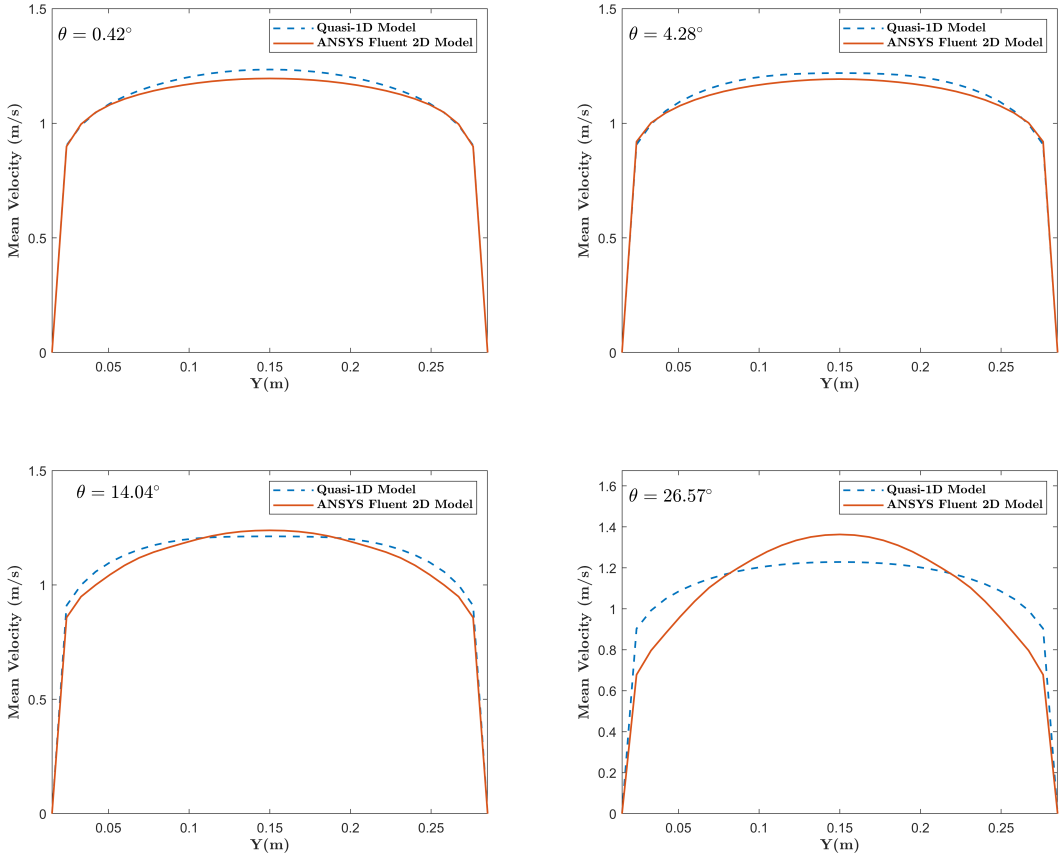

Fig. 1.19: Comparison of mean velocity profiles of Quasi-1D and ANSYS Fluent 2D models at $\frac{x}{L} = 0.2$

An important aspect of any numerical framework is its computational efficiency with respect to the grid resolution. As mentioned before, one of the main incentives to develop the quasi-1D model was its less computational cost compared with the 2D model. To investigate this, the simulation of Case1 was repeated using both the quasi-1D and ANSYS Fluent 2D models for a set of increasing numbers stream-wise grid cells N_x (from 500 to 25000), and the corresponding CPU times, as a measure of the computational cost, were recorded after 100 time steps. Fig. 1.20 displays how the CPU time of each model varies as a function of N_x (note that both axes have logarithmic scale). The two graphs should not be exactly compared since, for example, the definitions of the convergence criterion in the quasi-1D code and ANSYS Fluent are different, or there is still room to optimize the quasi-1D code, which is not in the scope of this work, as it is focused on the proof of concept of the quasi-1D approach. However, of primary interest here is the trend based on which the CPU time of each model depends on the number of grid cells. As it is seen, the CPU time of the ANSYS Fluent scales roughly with $N_x^{1.6}$ whereas that of the quasi-1D code varies linearly with N_x, which reveals that, from a certain number of grid cells on, the quasi-1D model will absolutely perform faster. This essentially owes to the fact that the 2D flow equations in the quasi-1D framework are converted to 1D equations, leading to tridiagonal configuration of the matrix of coefficients A in Eqn. (1.27) whose solution method is of first-order arithmetic complexity.

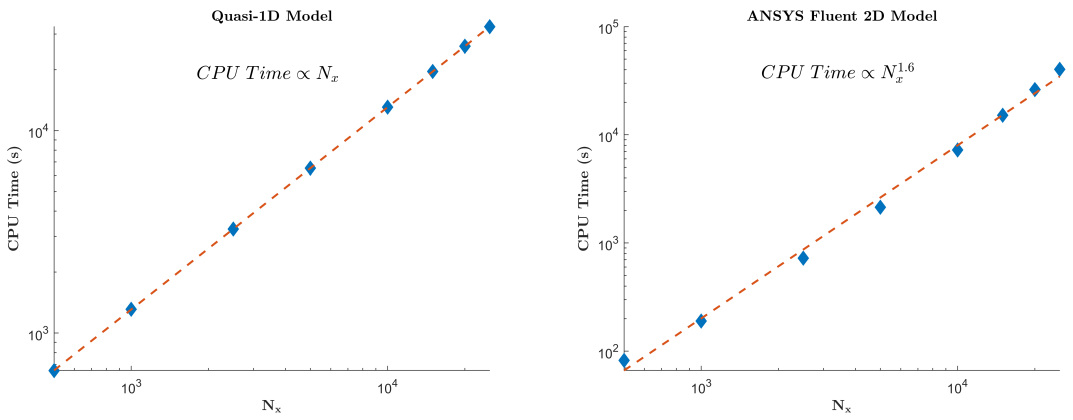

Fig. 1.20: CPU times of quasi-1D and ANSYS Fluent 2D Models as a function of the number of stream-wise grid cells N_x

It is also worth mentioning that a quasi-1D code is massively parallelizable simply because the set of equations for each cross section are solved independently from the other cross sections, implying that the cross-sectional profiles along the channel can be obtained in parallel if sufficient number of CPU nodes are available.

1.6 Conclusions

The steady-state flow of a single-phase incompressible fluid was modeled within the quasi-1D framework; the results and performance were validated and compared with those of the ANSYS Fluent 2D model as a benchmark. The following conclusions can be made from what was presented in this chapter:

- The results of the quasi-1D and ANSYS Fluent 2D models were in line with each other for the cases tested.
- For contraction angles smaller than $5°$, the quasi-1D model showed an error of less than 10% with respect to the ANSYS Fluent 2D model, which assures that the quasi-1D approach can be applied to the problem of asphaltenes transport and deposition in oil wells, where the stream-wise variation the deposit layer thickness is presumed to occur with a local contraction angle of much less than $1°$.
- The CPU time analysis revealed that the computational cost of the quasi-1D model increases linearly with the number of stream-wise grid cells (N_x), whereas that of the ANSYS Fluent 2D model scales roughly with $N_x^{1.6}$. This denotes that, from a certain number of grid cells on, the Quasi-1D code will definitely run faster than ANSYS Fluent.

Chapter 2

Particle Transport Modelling

This chapter begins with modelling the transport of a single-sized particulate phase in a turbulent channel flow using the Eulerian approach, which will then be generalized to particles of a continuous size distribution undergoing various physical processes, including nucleation, aggregation and breakage, by taking advantage of the population balance equation (PBE). Following a similar workflow as in chapter 1, the relevant 2D governing equations will be presented and modified based on the quasi-1D strategy, followed by the corresponding discrete forms plus the iterative algorithms applied to solve them.

2.1 Eulerian Model (Two-Fluid Model)

One of the several methods that have been developed to model multi-phase flows is referred to as the Eulerian-Eulerian or two-fluid approach. The basis of this technique is the formulation of a set of conservation equations (mass and momentum) for each phase, which can be carried out by ensemble-averaging the continuity and Navier-Stokes equations. Since the averaged quantities exist every where in space, it is commonly said that the two-fluid model regards the dispersed phase (here particles) as a "continuum".

In the two-fluid model, the interaction between one phase with the others is accounted for via interphase forces that appear in the phase momentum equations and need to be closed using empirical relations. This work is based on the one-way coupling assumption, stating that the continuous phase poses force on and is not influenced by the particulate phase, and no interactive forces also exist between the particles themselves. The continuity and momentum equations for the phase p are as follows:

$$\frac{\partial \alpha_p}{\partial t} + \frac{\partial(\alpha_p \langle U_p \rangle)}{\partial x} + \frac{\partial(\alpha_p \langle V_p \rangle)}{\partial y} = 0 \tag{2.1}$$

$$\begin{aligned} &\frac{\partial(\alpha_p \langle U_p \rangle^2)}{\partial x} + \frac{\partial(\alpha_p \langle V_p \rangle \langle U_p \rangle)}{\partial y} + \frac{\partial(\alpha_p \langle U_p' U_p' \rangle)}{\partial x} + \frac{\partial(\alpha_p \langle V_p' U_p' \rangle)}{\partial y} \\ &\qquad = \frac{18\nu\alpha_p}{D_p^2}(\langle U_{cp} \rangle - \langle U_p \rangle) - \frac{18\nu\nu_t}{D_p^2 \delta_{sc}} \frac{\partial \alpha_p}{\partial x} \end{aligned} \tag{2.2}$$

$$\begin{aligned} &\frac{\partial(\alpha_p \langle U_p \rangle \langle V_p \rangle)}{\partial x} + \frac{\partial(\alpha_p \langle V_p \rangle^2)}{\partial y} + \frac{\partial(\alpha_p \langle U_p' V_p' \rangle)}{\partial x} + \frac{\partial(\alpha_p \langle V_p' V_p' \rangle)}{\partial y} \\ &\qquad = -\frac{18\nu\alpha_p}{D_p^2} \langle V_p \rangle - \frac{18\nu\nu_t}{D_p^2 \delta_{sc}} \frac{\partial \alpha_p}{\partial y} \end{aligned} \tag{2.3}$$

where the angle brackets denote ensemble average, α_p is particle volume fraction, $\langle U_p \rangle$ particle mean velocity in the stream-wise direction, $\langle V_p \rangle$ particle mean velocity in the cross-stream direction, $\langle U_{cp} \rangle$ stream-wise mean flow velocity at the particle position and D_p particle diameter and δ_{sc} the turbulent schmidt number, which takes the value of 0.7 in case of perfect-tracer particles. These equations are comparable to the Reynolds-averaged continuity and Navier-Stokes equations, plus some extra terms such as stokes drag (first term on the right-hand side of the phase momentum equations) and drift flux (second term on the right-hand side of the phase momentum equations) that represent the physical forces and mechanisms accounting for the particles motion. Remember that the fluid flow is presumed not to occur in the cross-stream direction, which is the reason why the term $\langle V_{cp} \rangle$ does not appear in Eqn. (2.3). Moreover, similar to the way of achieving the steady state for the single-phase fluid flow in chapter 1, the steady state for the particles transport will be attained by considering a pseudo time term in the phase continuity equation and solving for the particulate phase characteristics until they do not vary in time. However, there is no need to incorporate the time term in the phase momentum equations as well, assuming that the forces acting on the particles are instantly at equilibrium.

When studying particle-laden flows, it is usually of high interest to discover how the particles tend to move in the cross-stream direction and eventually contribute to the total flux of deposition at the wall. Eqn. (2.3). accounts for the particles cross-stream movement under the two following mechanisms:

- **Turbophoresis** (last term on the left-hand side): Based on this mechanism, uniformly distributed particles tend to move towards the region with less turbulence intensity.
- **Drift Flux** (last term on the right-hand side): This mechanism causes the particles in a medium with homogeneous turbulent intensity to move towards the region with lower particle concentration.

These mechanisms are also present in the stream-wise direction but are expected to play a minor role since the particles are mainly under the influence of the drag force exerted by the mean flow (the first term on the right-hand side of Eqn. (2.2)).

Assuming that the particle fluctuations are determined by the turbulent fluctuations, the local equilibrium model can be used to close the components of the particle-phase Reynolds stress as follows:

$$\begin{aligned} \langle U_p' U_p' \rangle &= \Gamma \langle U_c' U_c' \rangle \\ \langle V_p' U_p' \rangle &= \Gamma \langle V_c' U_c' \rangle \\ \langle V_p' V_p' \rangle &= \Gamma \langle V_c' V_c' \rangle \end{aligned} \tag{2.4}$$

where the coefficient Γ is given by:

$$\Gamma = \frac{T_t}{T_t + \tau_p} \tag{2.5}$$

The turbulence time scale T_t and the particle relaxation time τ_p are also computed from the expressions below:

$$T_t = \sqrt{\frac{2}{3}} C_\mu \frac{k}{\varepsilon} \tag{2.6}$$

$$\tau_p = \frac{\rho_p D_p^2}{18\mu_c} \tag{2.7}$$

In case of very small particles, the relaxation time is much smaller than the turbulence time scale, implying that the particles will completely adjust to the turbulence ($\Gamma \approx 1$). However, very large particles will not be influenced by the turbulent fluctuations ($\Gamma \approx 0$). Note that the usage of this model is not essential to this work, and other closure relations could be used as well.

2.2 Population Balance Equation

In contrary to what discussed above, now suppose that the particulate phase is characterized by a continuous distribution of sizes and subject to various processes including nucleation, aggregation and breakage. In such a case, the continuity equation in the Eulerian model should be replaced with the population balance equation (PBE).

2.2.1 Particle Size Distribution

Any population of particles can be described by a unique particle size distribution (PSD), an example of which can be found in Fig. 2.1.

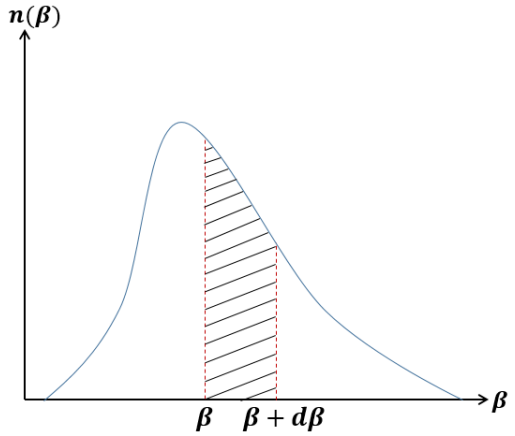

Fig. 2.1: An example of particle size distribution

In this figure, β represents a size-related property such as volume (V) or length (L), and $n(\beta)$ is called the number density function, based on which the particles number density ω within the size range $(\beta, \beta + \mathrm{d}\beta)$ can be computed as:

$$\omega(\beta, \beta + \mathrm{d}\beta) = n(\beta)\mathrm{d}\beta \tag{2.8}$$

From now on in this work, the length of the particles is chosen to be their size property. The characteristics of a PSD can be described by its moments, defined as:

$$m_k = \int_0^\infty L^k n(L)\mathrm{d}L \qquad k = 0, 1, ... \tag{2.9}$$

where k refers to the order of the moment. It is seen, for example, that m_0 represents the total number density of the particles, m_1 equals the mean of the PSD and so on. Therefore, one will be

able to reconstruct the PSD if its moments are known, which will be more elaborated on later in this section.

2.2.2 Gaussian Quadrature Rule

According to the Gaussian Quadrature rule (see e.g. Mukhtar et al., 2012), the one-dimensional integral of any function $f(x)$, defined over the domain (a, b) and weighted by an arbitrary non-negative function $\psi(x)$, can be approximated as follows:

$$I = \int_a^b \psi(x) f(x) \mathrm{d}x \approx \sum_{i=1}^{N} \omega_i f(x_i) \tag{2.10}$$

where N is the number of quadrature points, and ω_i is the weight corresponding to the quadrature abscissa x_i (see Fig. 2.2 as an example).

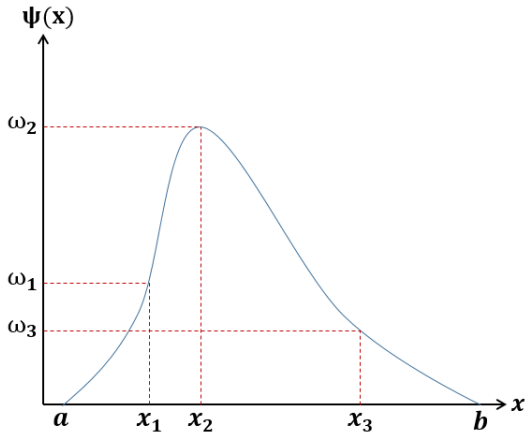

Fig. 2.2: Gaussian quadrature abscissas and weights

If the number density function $n(L)$ is chosen to be the weight function, Eqn. (2.10) for any particle length function $f(L)$ turns into:

$$I = \int_a^b n(L) f(L) \mathrm{d}L \approx \sum_{i=1}^{N} \omega_s f(L_s) \tag{2.11}$$

where ω_s and L_s are the quadrature weights and abscissas of the corresponding PSD. This equation is very useful, for example, in approximating the moments of the PSD as below:

$$m_k = \int_0^\infty L^k n(L) \mathrm{d}L \approx \sum_{s=1}^{N} \omega_s L_s^k \tag{2.12}$$

2.2.3 Formulation of Population Balance Equation

In order to identify a population of particles at any position in space and time, it is only needed to determine the corresponding PSD at that position. This comes true using the population balance

equation, which is essentially a transport equation for the number density function. According to Marchisio et al., 2007, the length-based form of the PBE reads:

$$\frac{\partial n(L)}{\partial t} + \frac{\partial\Big(\langle U_p|L\rangle n(L)\Big)}{\partial x} + \frac{\partial\Big(\langle V_p|L\rangle n(L)\Big)}{\partial y} = S(L) \tag{2.13}$$

where $\langle U_p|L\rangle$ and $\langle V_p|L\rangle$ are the mean velocity of the particles with length L in the stream-wise and cross-stream directions, respectively. The source term $S(L)$ can be written as follows:

$$S(L) = \overbrace{\frac{\partial n(L)}{\partial t}\bigg|_{Nuc}}^{\text{I}} + \overbrace{\frac{L^2}{2}\int_0^L E\Big((L^3-\lambda^3)^{\frac{1}{3}},\lambda\Big)\frac{\beta\Big((L^3-\lambda^3)^{\frac{1}{3}},\lambda\Big)}{(L^3-\lambda^3)^{\frac{1}{3}}} n\Big((L^3-\lambda^3)^{\frac{1}{3}}\Big)n(\lambda)\mathrm{d}L}^{\text{II}}$$
$$\overbrace{-n(L)\int_0^\infty \beta(L,\lambda)n(\lambda)\mathrm{d}\lambda}^{\text{III}} + \overbrace{\int_L^\infty a(\lambda)b(L|\lambda)n(\lambda)\mathrm{d}\lambda}^{\text{IV}} - \overbrace{a(L)n(L)}^{\text{V}}$$

which primarily consists of 5 terms, introduced along with the respective parameters below:

I: Nucleation particle size distribution (NPSD)

II: Formation of particles with size L from aggregation of smaller ones

- $\beta(L,\lambda)$: Rate of collision of particles with sizes L and λ (Collision Kernel)
- $E(L,\lambda)$: Collision efficiency of particles with sizes L and λ

III: Collision of particles of size L with any others leading to formation of larger aggregates

IV: Formation of particles with size L from breakage of larger aggregates

- $a(\lambda)$: Rate of breakage of particles with size λ (Breakage Kernel)
- $b(L|\lambda)$: Number of particles with size L formed from breakage of an aggregate with size λ (Fragment Distribution Function)

V: Breakage of particles with size L

In case of single-sized nucleating particles, the NPSD can be modeled using the Dirac delta function as:

$$\frac{\partial n(L)}{\partial t}\bigg|_{Nuc} = J_0\delta(L-L_0)$$

where J0 is the nucleation rate, and L0 indicates the size of the nucleating particles. In this work, the nucleation process is presumed to take place over the size range (L_a, L_b), which is taken into account via approximating the delta function by a step function (Fig. 2.3). However, note that any choices other than the step function could also be made.

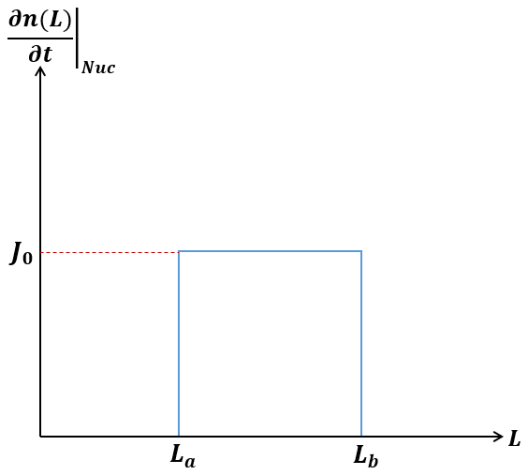

Fig. 2.3: Approximation of nucleation particle size distribution

2.2.4 Solution Methods of Population Balance Equation

The following are a number of the available techniques used to solve the PBE:

- **Discrete Method**: This method discretizes the PBE into a finite number of size intervals, for each of which the PDS can be directly calculated. It is useful particularly when the whole particle size range is known a priory and does not span more than two or three orders of magnitude. However, it is computationally expensive if a large number of intervals is needed (ANSYS Fluent 12.0 manual).

- **Standard method of moments (SMM)**: In this approach, the PBE is transformed into a set of transport equations for the moments of the PSD. It is generally sufficient to solve for only a few first moments of the PSD, typically up to the order three to six, which may provide a significant reduction in the number of equations to be solved compared with the discrete approach. Note also that the moment equations are formulated in a closed form involving only functions of the moments themselves, however, this exact closure requirement poses a serious limitation, as aggregation (with the exception of the constant aggregation kernel) and breakage phenomena cannot be written as functions of moments (ANSYS Fluent 12.0 manual).

- **Quadrature method of moments (QMOM)**: This method also deals with the transport equations for the moments of the PSD and has a similar advantage as SMM in terms of computational cost. However, the exact closures needed by SMM are replaced with approximate closures using the Gaussian Quadrature rule, which allows application of the QMOM to a broad range of phenomena including aggregation and breakage, without any limitations (ANSYS Fluent 12.0 manual). The main drawback of this method is that it assigns the whole particle range a uniform velocity field based on the mean particle size, which becomes problematic especially in case of multi-variate distribution functions.

- **Direct quadrature method of moments (DQMOM)**: In this method, a set of transport equations are worked out directly for the quadrature abscissas and weights of the PSD instead

of its moments. Each quadrature abscissa is assumed to occupy an independent velocity field, which allows to address the multi-variate PSD′s as well. A thorough explanation on the DQMOM will be given in the next subsection, as this approach will be employed in this study.

2.2.5 Direct Quadrature Method of Moments (DQMOM)

The outline of the DQMOM has been summarized below:

- Solving the transport equations for the quadrature weights and abscissas of the PSD.
- Obtaining the moments of the PSD using its quadrature weights and abscissas.
- Reconstructing the PSD from its moments.

Derivation of the transport equations for the quadrature abscissas and weights of the PSD starts with modelling the number density function $n(L)$ as a summation of weighted Dirac delta functions:

$$n(L) = \sum_{s=1}^{N} \omega_s \delta(L - L_s) \tag{2.14}$$

where N is the number of delta functions and ω_s is the weight of node s. In other words, this model divides the whole particle range into N separate classes, each represented by the characteristic length L_s and number density ω_s. It should be noted that L_s and ω_s are essentially the same as the abscissas and weights of the Gaussian quadrature rule, as is also implied by the name of the method. Theoretically speaking, the higher the number of nodes N, the more accurate the DQMOM will be but at the expense of higher computational effort. In this study, the practical value of $N = 3$ is used, which most of the time leads to acceptable results with reasonable computational cost.

Substituting Eqn. (2.14) into Eqn. (2.13) and applying some mathematical manipulations (see Marchisio et al., 2005), the following transport equations can be worked out for the weights (ω_s) and the abscissas (L_s):

$$\frac{\partial \omega_s}{\partial t} + \frac{\partial(\langle U_p \rangle_s \omega_s)}{\partial x} + \frac{\partial(\langle V_p \rangle_s \omega_s)}{\partial y} = a_s \tag{2.15}$$

$$\frac{\partial(\omega_s L_s)}{\partial t} + \frac{\partial(\langle U_p \rangle_s \omega_s L_s)}{\partial x} + \frac{\partial(\langle V_p \rangle_s \omega_s L_s)}{\partial y} = b_s \tag{2.16}$$

The source terms a_s and b_s are obtained from the following set of $2N$ equations:

$$(1-k)\sum_{s=1}^{N} L_s^k a_s + k\sum_{s=1}^{N} L_s^{k-1} b_s = S_k^N \qquad k = 0, 1, ..., 2N-1 \tag{2.17}$$

where:

$$S_k^N = \frac{(L_b^{k+1} - L_a^{k+1})J_0}{(k+1)(L_b - L_a)} + \frac{1}{2}\int_0^\infty\int_0^\infty (L^3 + \lambda^3)^{\frac{k}{3}} \beta(L, \lambda) n(L) n(\lambda) \mathrm{d}L \mathrm{d}\lambda$$

$$- \int_0^\infty L^k n(L) \int_0^\infty \beta(L, \lambda) n(\lambda) \mathrm{d}\lambda \mathrm{d}L + \int_0^\infty a(\lambda) n(\lambda) b^k(\lambda) \mathrm{d}\lambda - \int_0^\infty a(L) L^k n(L) \mathrm{d}L$$

The new term $b^k(\lambda)$ is called the daughter distribution function and defined as:

$$b^k(\lambda) = \int_0^\infty L^k b(L|\lambda)\mathrm{d}L$$

As an example, Eqn. (2.17) for $N = 3$ can be written in the matrix form below:

$$\begin{pmatrix} 1 & 1 & 1 & 0 & 0 & 0 \\ 0 & 0 & 0 & 1 & 1 & 1 \\ -L_1^2 & -L_2^2 & -L_3^2 & 2L_1 & 2L_2 & 2L_3 \\ -2L_1^3 & -2L_2^3 & -2L_3^3 & 3L_1^2 & 3L_2^2 & 3L_3^2 \\ -3L_1^4 & -3L_2^4 & -3L_3^4 & 4L_1^3 & 4L_2^3 & 4L_3^3 \\ -4L_1^5 & -4L_2^5 & -4L_3^5 & 5L_1^4 & 5L_2^4 & 5L_3^4 \end{pmatrix} \begin{pmatrix} a_1 \\ a_2 \\ a_3 \\ b_1 \\ b_2 \\ b_3 \end{pmatrix} = \begin{pmatrix} S_0^3 \\ S_1^3 \\ S_2^3 \\ S_3^3 \\ S_4^3 \\ S_5^3 \end{pmatrix} \tag{2.18}$$

Taking advantage of Eqn. (2.11), all the integral terms present in S_k^N can be approximated by summations as follows:

$$S_k^N = \frac{(L_b^{k+1} - L_a^{k+1})J_0}{(k+1)(L_b - L_a)} + \frac{1}{2}\sum_{s=1}^{N}\sum_{t=1}^{N}\omega_s\omega_t(L_s^3 - L_t^3)^{\frac{k}{3}}\beta(L_s, L_t)$$

$$-\sum_{s=1}^{N}\sum_{t=1}^{N}\omega_s\omega_t L_s^k\beta(L_s, L_t) + \sum_{s=1}^{N}\omega_s a(L_s)b^k(L_s) - \sum_{s=1}^{N}\omega_s L_s^k a(L_s)$$

Note also that the mean velocities appearing in the advection terms of Eqn. (2.15) and (2.16) are acquired from Eqn. (2.2) and (2.3), where the volume fraction of each particle class can be calculated from:

$$\alpha_s = \frac{\pi}{6}L_s^3\omega_s \tag{2.19}$$

2.2.6 PSD Reconstruction

Once the quadrature weights and abscissas of the PSD are obtained from the respective transport equations in the DQMOM, the moments of the PSD can be acquired from Eqn. (2.12), which are used to reconstruct the PSD. Different possible methods have been developed allowing reconstruction of a PSD from its moments (John et al., 2007) such as:

- **Prescribed function method**: The fastest and easiest way of constructing a PSD, knowing only some of its moments, is fitting it to a prescribed mathematical function. This method is limited to simple shapes and also requires a prior knowledge about the solution of the problem.

- **Spline-based reconstruction**: In this method, the whole particle size range is divided into a number of intervals based on the number of moments available. Then, the shape of the PSD will be approximated by a piecewise polynomial function. The advantage of this methos is that no prior assumptions are needed about the shape of the PSD, and any arbitrary number of moments can be used. However, it is computationally more expensive than the prescribed function method, and also the system of equations solved to obtain the polynomial coefficients is very ill-conditioned.

In this work, the prescribed function method will be used due to its computational efficiency and simple implementation. As mentioned above, the choice of the mathematical function in this method is completely problem-dependent. For example, consider a population of particles, which are nucleated with a symmetric size distribution and then continue growing in size due to aggregation, as applies to the asphaltenes transport in oil wells discussed in chapter 3. In this case, as the transport process goes on, the PSD will keep on being skewed more and more towards the larger particles. Therefore, in order to describe the shape of such a PSD based on this prior knowledge, Gamma function would be a good choice since it take various shapes depending on the skewness and kurtosis values deduced from the respective moment data (Heinz, 2003):

$$f(x) = \frac{\mu^{\mu} x^{(\mu-1)} exp(-\mu x/\overline{x})}{\Gamma(\mu)\overline{x}^{\mu}} \tag{2.20}$$

where:

$$\mu = \frac{\overline{x}^2}{\sigma^2} \qquad \text{and} \qquad \Gamma(\mu) = \int_0^{\infty} z^{\mu-1} e^z \mathrm{d}z$$

The mean size $\overline{x}$ and the standard deviation σ are obtained from the first three moments of the PSD as:

$$\overline{x} = \frac{m_1}{m_0} \qquad \text{and} \qquad \sigma = \frac{m_1}{m_0}\sqrt{\frac{m_0 m_2}{m_1} - 1}$$

It should be noted that m_0 is not unity since, by definition, it is equal to the total number of particles per unit volume.

2.3 Quasi-1D Model for Particulate Phase

The transport of a population of particles with a continuous size distribution in turbulent flow was modeled using the PBE coupled to the Eulerian model. Now, the quasi-1D idea will be applied again to convert the 2D equations into separate 1D equations in the stream-wise and cross-stream directions, which can be solved in an iterative fashion.

2.3.1 Stream-Wise 1D Equations

Integrating Eqn. (2.2), (2.3), (2.15) and (2.16) with respect to y from 0 to H and then applying the averaging definition, presented by Eqn. (1.14), yields:

$$\frac{\partial\Big(F_{\mathrm{U1s}}H\overline{\alpha}_s\langle\overline{U}_p\rangle_s^2\Big)}{\partial x}-\Big(\alpha_s\langle V_p\rangle_s\langle U_p\rangle_s\Big)_0+\frac{\partial\Big(F_{\mathrm{U2s}}H\overline{\alpha}_s\langle\overline{U_p'U_p'}\rangle_s\Big)}{\partial x}=\frac{18F_{\mathrm{U3s}}H\nu\overline{\alpha}_s}{\overline{L}_p^2}\langle\overline{U}_{cp}\rangle_s$$
$$-\frac{18F_{\mathrm{U4s}}H\nu\overline{\alpha}_s}{\overline{L}_p^2}\langle\overline{U}_p\rangle_s-\frac{18F_{\mathrm{U5s}}H\nu\overline{\nu}_t}{\overline{L}_s^2\delta_{sc}}\frac{\partial\overline{\alpha}_s}{\partial x} \tag{2.21}$$

$$\frac{\partial\Big(F_{\mathrm{V1s}}H\overline{\alpha}_s\langle\overline{U}_p\rangle_s\langle\overline{V}_p\rangle_s\Big)}{\partial x}-\Big(\alpha_s\langle V_p\rangle_s^2\Big)_0+\frac{\partial\Big(F_{\mathrm{V2s}}H\overline{\alpha}_s\langle\overline{U_p'V_p'}\rangle_s\Big)}{\partial x}=-\frac{18F_{\mathrm{V3s}}H\nu\overline{\alpha}_s}{\overline{L}_s^2}\langle\overline{V}_p\rangle_s$$
$$-\frac{18F_{\mathrm{V4s}}H\nu\overline{\nu}_t}{\overline{L}_s^2\delta_{sc}}\frac{\overline{\partial\alpha_s}}{\partial y} \tag{2.22}$$

$$\frac{\partial\Big(H\overline{\omega}_s\Big)}{\partial t}+\frac{\partial\Big(F_{\omega s}H\langle\overline{U}_p\rangle_s\overline{\omega}_s\Big)}{\partial x}-\Big(\langle V_p\rangle_s\omega_s\Big)_0=H\bar{a}_s \tag{2.23}$$

$$\frac{\partial\Big(F_{\mathrm{L1s}}H\overline{\omega}_s\overline{L}_s\Big)}{\partial t}+\frac{\partial\Big(F_{\mathrm{L2s}}H\langle\overline{U}_p\rangle_s\overline{\omega}_s\overline{L}_s\Big)}{\partial x}-\Big(\langle V_p\rangle_s\omega_sL_s\Big)_0=H\bar{b}_s \tag{2.24}$$

which are used to attain the stream-wise distributions of the average particle mean velocities $\langle\overline{U}_p\rangle_s$ and $\langle\overline{V}_p\rangle_s$, number density $\overline{\omega}_s$ and length $\overline{L}_s$, respectively. The terms bearing the subscript 0 are in fact fluxes at the wall and behave exactly in the same way as the wall shear-stress does in Eqn. (1.17). The average volume fraction $\overline{\alpha}_s$ appearing in Eqn. (2.21) and (2.22) is calculated from:

$$\overline{\alpha}_s=\frac{\pi}{6}F_{\alpha s}\overline{L}_s^3\overline{\omega}_s \tag{2.25}$$

and the source terms $\bar{a}_s$ and $\bar{b}_s$ on the right-hand side of in Eqn. (2.23) and (2.24) can be obtained from the averaged form of Eqn. (2.17):

$$F_{\mathrm{aks}}H(1-k)\sum_{s=1}^{N}\overline{L}_s^k\bar{a}_s+F_{\mathrm{bks}}Hk\sum_{s=1}^{N}\overline{L}_s^{k-1}\bar{b}_s=H\overline{S}_k^N \tag{2.26}$$

where:

$$\overline{S}_k^N=\frac{(F_{\mathrm{Pbk}}\overline{L}_b^{k+1}-F_{\mathrm{Pak}}\overline{L}_a^{k+1})J_0}{(k+1)(\overline{L}_b-\overline{L}_a)}+\frac{1}{2}\sum_{s=1}^{N}\sum_{t=1}^{N}F_{\mathrm{ABkst}}\,\overline{\omega}_s\overline{\omega}_t(\overline{L}_s^3-\overline{L}_t^3)^{\frac{k}{3}}\beta(\overline{L}_s,\overline{L}_t)$$
$$-\sum_{s=1}^{N}\sum_{t=1}^{N}F_{\mathrm{ADkst}}\,\overline{\omega}_s\overline{\omega}_t\overline{L}_s^k\beta(\overline{L}_s,\overline{L}_t)+\sum_{s=1}^{N}F_{\mathrm{BBks}}\,\overline{\omega}_sa(\overline{L}_s)b^k(\overline{L}_s)-\sum_{s=1}^{N}F_{\mathrm{BDks}}\,\overline{\omega}_s\overline{L}_s^ka(\overline{L}_s)$$

All the F parameters are the averaging separation factors, similar to the one used to convert the mean squared flow velocity to its squared mean in section 1.3. One should notice that only the subscripts k, s and t are counted over, and the rest have been used for naming purpose.

2.3.2 Cross-Stream 1D Equations

Lumping the terms with the x-derivative in Eqn. (2.2), (2.3), (2.15) and (2.16) into a "source term" Ψ, which is assumed to be uniform with respect to y, the following 1D equations in the cross-stream direction are worked out:

$$\frac{\partial\Big(\alpha_s\langle V_p\rangle_s\langle U_p\rangle_s\Big)}{\partial y}+\frac{\partial\Big(\alpha_s\langle V_p'U_p'\rangle_s\Big)}{\partial y}=\frac{18\nu\alpha_s}{L_s^2}\Big(\langle U_{cp}\rangle_s-\langle U_p\rangle_s\Big)+\Psi_U \tag{2.27}$$

$$\frac{\partial\Big(\alpha_s\langle V_p\rangle_s^2\Big)}{\partial y}+\frac{\partial\Big(\alpha_s\langle V_p'V_p'\rangle_s\Big)}{\partial y}=-\frac{18\nu\alpha_s}{L_s^2}\langle V_p\rangle_s-\frac{18\nu\nu_t}{L_p^2\delta_{sc}}\frac{\partial\alpha_s}{\partial y}+\Psi_V \tag{2.28}$$

$$\frac{\partial\omega_s}{\partial t}+\frac{\partial(\langle V_p\rangle_s\omega_s)}{\partial y}=a_s+\Psi_\omega \tag{2.29}$$

$$\frac{\partial(\omega_s L_s)}{\partial t}+\frac{\partial(\langle V_p\rangle_s\omega_s L_s)}{\partial y}=b_s+\Psi_L \tag{2.30}$$

which should be solved simultaneously for each cross-section to obtain the profiles of the particle mean velocities $\langle U_p\rangle_s$ and $\langle V_p\rangle_s$, length L_s and number density ω_s. This is carried out, in the same way as Eqn. (1.18) was solved in chapter 1, by varying the value of Ψ in each equation until achieving a profile for the respective variable whose cross-sectional average equals the value provided by the corresponding stream-wise 1D equation at the x-position of interest. Once the profiles of all the variables are constructed along the channel, the stream-wise distribution of the wall fluxes (terms with subscript 0) in Eqn. (2.21), (2.22), (2.23) and (2.24) will be updated. Note that the initial iteration guess for each Ψ can be estimated from:

$$\Psi_{U-Initial}=-\frac{\partial\Big(H\overline{\alpha}_s\langle\overline{U}_p\rangle_s^2\Big)}{\partial x}-\frac{\partial\Big(H\overline{\alpha}_s\langle\overline{U_p'U_p'}\rangle_s\Big)}{\partial x}-\frac{18H\nu\overline{\nu}_t}{\overline{L}_s^2\delta_{sc}}\frac{\partial\overline{\alpha}_s}{\partial x} \tag{2.31}$$

$$\Psi_{V-Initial}=-\frac{\partial\Big(H\overline{\alpha}_s\langle\overline{U}_p\rangle_s\langle\overline{V}_p\rangle_s\Big)}{\partial x}-\frac{\partial\Big(H\overline{\alpha}_s\langle\overline{U_p'V_p'}\rangle_s\Big)}{\partial x} \tag{2.32}$$

$$\Psi_{\omega-Initial}=-\frac{\partial\Big(H\langle\overline{U}_p\rangle_s\overline{\omega}_s\Big)}{\partial x} \tag{2.33}$$

$$\Psi_{L-Initial}=-\frac{\partial\Big(H\langle\overline{U}_p\rangle_s\overline{\omega}_s\overline{L}_s\Big)}{\partial x} \tag{2.34}$$

2.3.3 Boundary Conditions

The following are among the possible boundary conditions for the particulate phase equations, which can be applied depending on the problem under study:

- At the inlet, a fixed flux of particles can be specified to enter the domain with a velocity equal to that of the carrier fluid.

- At the outlet, zero derivative of the particles stream-wise and cross-stream mean velocities can be imposed.
- Symmetry condition can be applied on the centerline of the channel, unless the effect of the gravity is taken into account in the cross-stream direction.
- In proximity of the wall, it can be assumed that the particles move towards the wall without any change in their velocity (free-flight boundary condition), which is especially the case for large particles. However, for small particles, the free-flight condition should be modified to incorporate the influence of the turbulent fluctuations as well.

2.3.4 Iteration Procedure

The following flowchart explains the iterative procedure considered between the stream-wise and cross-stream 1D equations to arrive at a convergent solution:

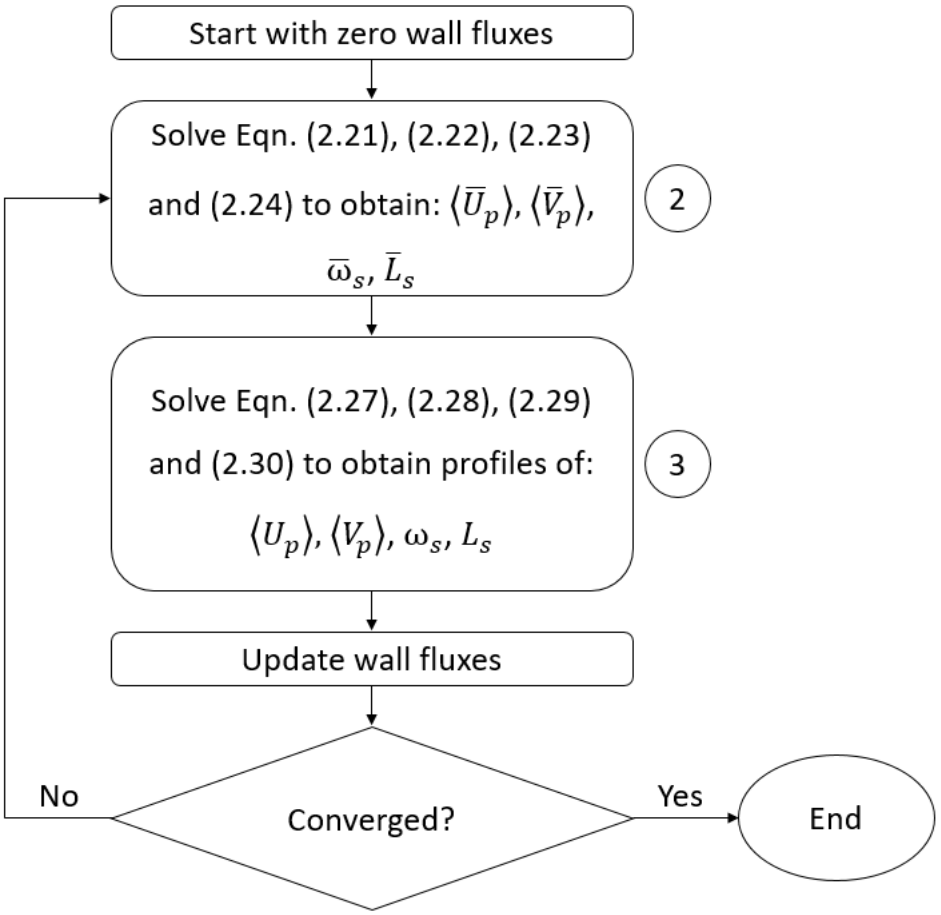

Fig. 2.4: Iteration procedure for transport of particulate phase

Each of the steps 2 and 3 consists of inner iteration, which will be explained in the next section.

2.4 Numerical Solution for Particulate Phase Equations

Following the numerical approach applied to the single-phase flow equations in chapter 1, the particulate phase 1D equations in the stream-wise and cross-stream directions will be discretized on the same grid stencils as in Fig. 1.7 and Fig. 1.10. The only difference here is that the spatial derivatives in the transport equations for L_s and ω_s are approximated using first-order upwind scheme. In order to understand this scheme, consider the spatial derivative below as an example:

$$\frac{\partial(U\Omega)}{\partial x}$$

where Ω is the quantity to be transported by the velocity U in the stream-wise direction. This derivative can be discretized for the cell center i as follows:

$$\frac{U_{i+\frac{1}{2}}\Omega_{i+\frac{1}{2}} - U_{i-\frac{1}{2}}\Omega_{i-\frac{1}{2}}}{\Delta x}$$

Supposing that the transport velocity is positive ($U > 0$), the information of the quantity Ω at the cell interfaces $i-\frac{1}{2}$ and $i+\frac{1}{2}$ is coming from the corresponding upstream cell centers. In other words, the values $\Omega_{i-\frac{1}{2}}$ and $\Omega_{i+\frac{1}{2}}$ should be adopted from the cell centers $i-1$ and i, respectively. This is called the first-order upwind scheme, which can be written in its general mathematical form as:

$$\Omega_{i-\frac{1}{2}} = \begin{cases} \Omega_{i-1} & U_{i-\frac{1}{2}} \geq 0 \\ \Omega_i & U_{i-\frac{1}{2}} \leq 0 \end{cases} \quad and \quad \Omega_{i+\frac{1}{2}} = \begin{cases} \Omega_i & U_{i+\frac{1}{2}} \geq 0 \\ \Omega_{i+1} & U_{i+\frac{1}{2}} \leq 0 \end{cases}$$

2.4.1 Discrete Form of Stream-Wise 1D Equations

Below are the discrete forms of

Eqn. (2.21):

$$A_{i-\frac{1}{2}}\langle\overline{U}_p\rangle_{s_{i-\frac{1}{2}}} + A_{i+\frac{1}{2}}\langle\overline{U}_p\rangle_{s_{i+\frac{3}{2}}} + A_{i+\frac{3}{2}}\langle\overline{U}_p\rangle_{s_{i+\frac{3}{2}}} = B_{i+\frac{1}{2}} \tag{2.35}$$

where:

$$A_{i-\frac{1}{2}} = -\frac{F_{\mathrm{U1S}_i}H_i\overline{\alpha}_{s_i}\left(\langle\overline{U}_p\rangle_{s_{i-\frac{1}{2}}} + \langle\overline{U}_p\rangle_{s_{i+\frac{1}{2}}}\right)}{4\Delta x}$$

$$A_{i+\frac{1}{2}} = -\frac{F_{\mathrm{U1S}_i}H_i\overline{\alpha}_{s_i}\left(\langle\overline{U}_p\rangle_{s_{i-\frac{1}{2}}} + \langle\overline{U}_p\rangle_{s_{i+\frac{1}{2}}}\right)}{4\Delta x} + \left(\frac{18F_{\mathrm{U3S}}H\nu\overline{\alpha}_s}{\overline{L}_s^2}\right)_i + \frac{F_{\mathrm{U1S}_{i+1}}H_{i+1}\overline{\alpha}_{s_{i+1}}\left(\langle\overline{U}_p\rangle_{s_{i+\frac{1}{2}}} + \langle\overline{U}_p\rangle_{s_{i+\frac{3}{2}}}\right)}{4\Delta x}$$

$$A_{i+\frac{3}{2}} = \frac{F_{\mathrm{U1S}_{i+1}}H_{i+1}\overline{\alpha}_{s_{i+1}}\left(\langle\overline{U}_p\rangle_{s_{i+\frac{1}{2}}} + \langle\overline{U}_p\rangle_{s_{i+\frac{3}{2}}}\right)}{4\Delta x}$$

$$B_{i+\frac{1}{2}} = \left(\alpha_s \langle V_p \rangle_s \langle U_p \rangle_s\right)_{0_{i+\frac{1}{2}}} + \frac{\left(F_{\mathrm{U2S}} H \bar{\alpha}_s \langle \overline{U_p' U_p'} \rangle_s\right)_i}{\Delta x} - \frac{\left(F_{\mathrm{U2S}} H \bar{\alpha}_s \langle \overline{U_p' U_p'} \rangle_s\right)_{i+1}}{\Delta x} + \left(\frac{18 F_{\mathrm{U4S}} H \nu \bar{\alpha}_s}{\bar{L}_s^2} \langle \bar{U}_{cp} \rangle_s\right)_{i+\frac{1}{2}} - \left(\frac{18 F_{\mathrm{U5S}} H \nu \bar{\nu}_t}{\bar{L}_s^2 \sigma_{sc}} \frac{\partial \bar{\alpha}_s}{\partial x}\right)_{i+\frac{1}{2}}$$

Eqn. (2.22):

$$A_{i-1} \langle \bar{V}_p \rangle_{s_{i-1}} + A_i \langle \bar{V}_p \rangle_{s_i} + A_{i+1} \langle \bar{V}_p \rangle_{s_{i+1}} = B_i \tag{2.36}$$

where:

$$A_{i-1} = -\frac{F_{\mathrm{V1S}_{i-\frac{1}{2}}} H_{i-\frac{1}{2}} (\bar{\alpha}_{s_{i-1}} + \bar{\alpha}_{s_i}) \langle \bar{U}_p \rangle_{s_{i-\frac{1}{2}}}}{4 \Delta x}$$

$$A_i = -\frac{F_{\mathrm{V1S}_{i-\frac{1}{2}}} H_{i-\frac{1}{2}} (\bar{\alpha}_{s_{i-1}} + \bar{\alpha}_{s_i}) \langle \bar{U}_p \rangle_{s_{i-\frac{1}{2}}}}{4 \Delta x} + \left(\frac{18 F_{\mathrm{V3S}_i} H \nu \bar{\alpha}_s}{\bar{L}_s^2}\right)_i + \frac{F_{\mathrm{V1S}_{i+\frac{1}{2}}} H_{i+\frac{1}{2}} (\bar{\alpha}_{s_i} + \bar{\alpha}_{s_{i+1}}) \langle \bar{U}_p \rangle_{s_{i+\frac{1}{2}}}}{4 \Delta x}$$

$$A_{i+1} = \frac{F_{\mathrm{V1S}_{i+\frac{1}{2}}} H_{i+\frac{1}{2}} (\bar{\alpha}_{s_i} + \bar{\alpha}_{s_{i+1}}) \langle \bar{U}_p \rangle_{s_{i+\frac{1}{2}}}}{4 \Delta x}$$

$$B_i = \left(\alpha \langle V_p \rangle_s^2\right)_{0_i} + \frac{\left(F_{\mathrm{V2S}} H \bar{\alpha}_s \langle \overline{U_p' V_p'} \rangle_s\right)_{i-\frac{1}{2}}}{\Delta x} - \frac{\left(F_{\mathrm{V2S}} H \bar{\alpha}_s \langle \overline{U_p' V_p'} \rangle_s\right)_{i+\frac{1}{2}}}{\Delta x} - \left(\frac{18 F_{\mathrm{V4S}} H \nu \bar{\nu}_t}{\bar{L}_s^2 \sigma_{sc}} \overline{\frac{\partial \alpha_s}{\partial y}}\right)_i$$

Eqn. (2.23):

$$\left[-\frac{F_{\omega s_{i-\frac{1}{2}}} H_{i-\frac{1}{2}} \langle \bar{U}_p \rangle_{s_{i-\frac{1}{2}}}}{\Delta x}\right] \bar{\omega}_{s_{i-1}}^{n+1} + \left[\frac{H_i}{\Delta t} + \frac{F_{\omega s_{i+\frac{1}{2}}} H_{i+\frac{1}{2}} \langle \bar{U}_p \rangle_{s_{i+\frac{1}{2}}}}{\Delta x}\right] \bar{\omega}_{s_i}^{n+1} = \left(\frac{H_i}{\Delta t}\right) \bar{\omega}_{s_i}^{n} + \left(\langle V_p \rangle_s \omega_s\right)_{0_i} + H_i \bar{a}_{s_i} \tag{2.37}$$

Eqn. (2.24):

$$\left[-\frac{F_{\mathrm{L2S}_{i-\frac{1}{2}}} H_{i-\frac{1}{2}} \langle \bar{U}_p \rangle_{s_{i-\frac{1}{2}}} \bar{\omega}_{s_{i-1}}^{n+1}}{\Delta x}\right] \bar{L}_{s_{i-1}}^{n+1} + \left[\frac{F_{\mathrm{L1S}_i} H_i \bar{\omega}_{s_i}^{n+1}}{\Delta t} + \frac{F_{\mathrm{L2S}_{i+\frac{1}{2}}} H_{i+\frac{1}{2}} \langle \bar{U}_p \rangle_{s_{i+\frac{1}{2}}} \bar{\omega}_{s_i}^{n+1}}{\Delta x}\right] \bar{L}_{s_i}^{n+1} = \left(\frac{F_{\mathrm{L1S}_i} H_i \bar{\omega}_{s_i}^{n}}{\Delta t}\right) \bar{L}_{s_i}^{n} + \left(\langle V_p \rangle_s \omega_s L_s\right)_{0_i} + H_i \bar{b}_{s_i} \tag{2.38}$$

Note that the upstream always points towards the inlet since the particle mean velocity in the stream-wise direction is positive throughout the channel. Therefore, the upwind values of L_s and ω_s on any grid interface should be received from the corresponding back cell:

$$(\overline{\omega}_{s_{i+\frac{1}{2}}}, \overline{L}_{s_{i+\frac{1}{2}}}) = (\overline{\omega}_{s_i}, \overline{L}_{s_i}) \quad and \quad (\overline{\omega}_{s_{i-\frac{1}{2}}}, \overline{L}_{s_{i-\frac{1}{2}}}) = (\overline{\omega}_{s_{i-1}}, \overline{L}_{s_{i-1}})$$

The iteration procedure used to arrive at a convergent solution for the above equations is described in the following flowchart:

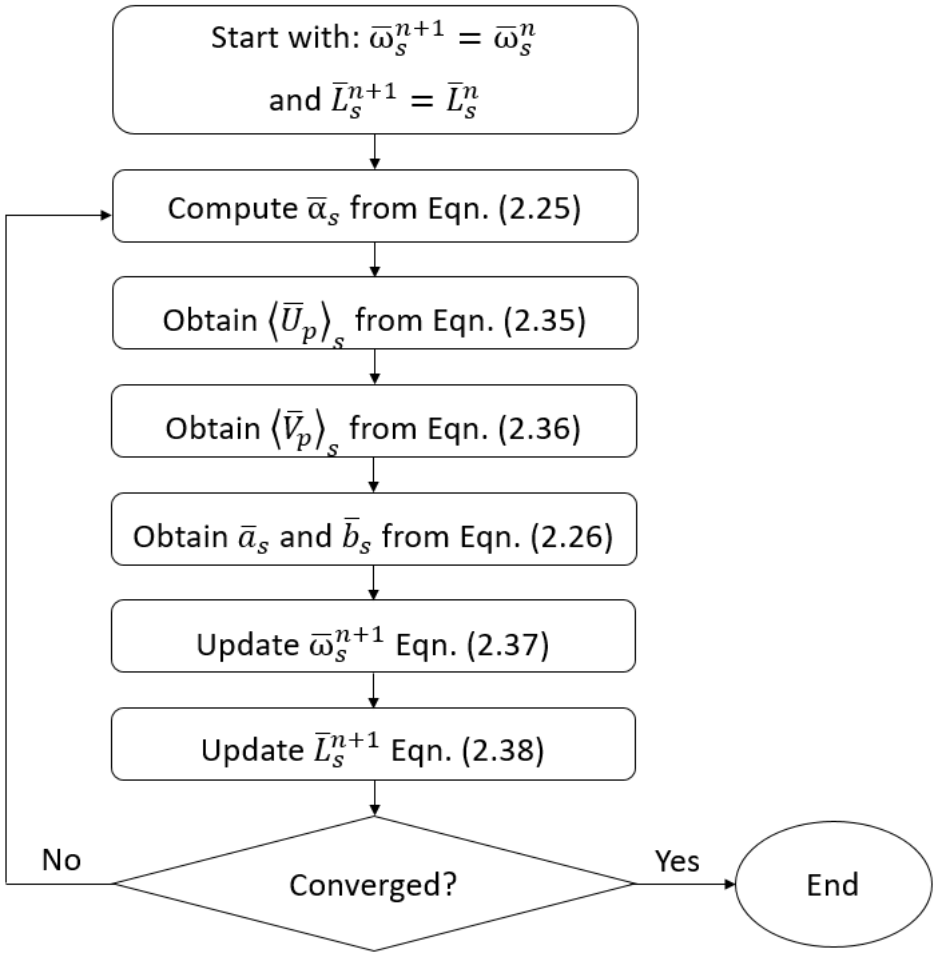

Fig. 2.5: Iteration procedure for stream-wise 1D equations

2.4.2 Discrete Form of Cross-Stream 1D Equations

Below are the discrete forms of

Eqn. (2.27):

$$A_{j-1}\langle U_p \rangle_{s_{j-1}} + A_j \langle U_p \rangle_{s_j} + A_{j+1}\langle U_p \rangle_{s_{j+1}} = B_j \tag{2.39}$$

where:

$$A_{j\text{-}1} = -\frac{(\alpha_{s_{j\text{-}1}} + \alpha_{s_j})\langle V_p \rangle_{s_{j\text{-}\frac{1}{2}}}}{4}$$

$$A_j = -\frac{(\alpha_{s_{j\text{-}1}} + \alpha_{s_j})\langle V_p \rangle_{s_{j\text{-}\frac{1}{2}}}}{4} + \left(\frac{18\nu\alpha_p \Delta y}{L_s^2}\right)_j + \frac{(\alpha_{s_j} + \alpha_{s_{j+1}})\langle V_p \rangle_{s_{j+\frac{1}{2}}}}{4}$$

$$A_{j+1} = \frac{(\alpha_{s_j} + \alpha_{s_{j+1}})\langle V_p \rangle_{s_{j+\frac{1}{2}}}}{4}$$

$$B_j = \left(\frac{18\nu\alpha_s \Delta y \langle U_{cs} \rangle}{L_s^2}\right)_j + \frac{(\alpha_{s_{j\text{-}1}} + \alpha_{s_j})\langle V_p' U_p' \rangle_{s_{j\text{-}\frac{1}{2}}}}{2} - \frac{(\alpha_{s_j} + \alpha_{s_{j+1}})\langle V_p' U_p' \rangle_{s_{j+\frac{1}{2}}}}{2} + \Psi_U \Delta y_j$$

Eqn (2.28):

$$A_{j-\frac{1}{2}} \langle V_p \rangle_{s_{j-\frac{1}{2}}} + A_{j+\frac{1}{2}} \langle V_p \rangle_{s_{j+\frac{1}{2}}} + A_{j+\frac{3}{2}} \langle V_p \rangle_{s_{j+\frac{3}{2}}} = B_{j+\frac{1}{2}} \tag{2.40}$$

where:

$$A_{j-\frac{1}{2}} = -\frac{\alpha_{s_j}\left(\langle V_p \rangle_{s_{j-\frac{1}{2}}} + \langle V_p \rangle_{s_{j+\frac{1}{2}}}\right)}{4}$$

$$A_{j+\frac{1}{2}} = -\frac{\alpha_{s_j}\left(\langle V_p \rangle_{s_{j-\frac{1}{2}}} + \langle V_p \rangle_{s_{j+\frac{1}{2}}}\right)}{4} + \left(\frac{18\nu\alpha_s \Delta y}{L_s^2}\right)_{j+\frac{1}{2}} + \frac{\alpha_{s_{j+1}}\left(\langle V_p \rangle_{s_{j+\frac{1}{2}}} + \langle V_p \rangle_{s_{j+\frac{3}{2}}}\right)}{4}$$

$$A_{j+\frac{3}{2}} = \frac{\alpha_{s_{j+1}}\left(\langle V_p \rangle_{s_{j+\frac{1}{2}}} + \langle V_p \rangle_{s_{j+\frac{3}{2}}}\right)}{4}$$

$$B_{j+\frac{1}{2}} = -\left(\frac{18\nu\nu_t}{L_s^2 \delta_{sc}}\right)_{j+\frac{1}{2}} (\alpha_{s_{j+1}} - \alpha_{s_j}) + \left(\alpha_s \langle V_p' V_p' \rangle_s\right)_j - \left(\alpha_s \langle V_p' V_p' \rangle_s\right)_{j+1} + \Psi_V \Delta y_{j+\frac{1}{2}}$$

Eqn. (2.29):

$$-\left(\frac{\langle V_p \rangle_{s_{j-\frac{1}{2}}}}{\Delta y_j}\right)\omega_{s_{j+r}}^{n+1} + \left(\frac{\Delta y_j}{\Delta t}\right)\omega_{s_j}^{n+1} + \left(\frac{\langle V_p \rangle_{s_{j+\frac{1}{2}}}}{\Delta y_j}\right)\omega_{s_{j+q}}^{n+1} = \left(\frac{\Delta y_j}{\Delta t}\right)\omega_{s_j}^{n} + \Psi_\omega \Delta y_j \tag{2.41}$$

Eqn. (2.30):

$$-\left(\frac{\langle V_p\rangle_{s_{j-\frac{1}{2}}}\omega_{s_{j+r}}^{n+1}}{\Delta y_j}\right)L_{s_{j+r}}^{n+1}+\left(\frac{\Delta y_j\omega_{s_j}^{n+1}}{\Delta t}\right)L_{s_j}^{n+1}+\left(\frac{\langle V_p\rangle_{s_{j+\frac{1}{2}}}\omega_{s_{j+q}}^{n+1}}{\Delta y_j}\right)L_{s_{j+q}}^{n+1}=\left(\frac{\Delta y_j\omega_{s_j}^{n}}{\Delta t}\right)L_{s_j}^{n}+\Psi_L\Delta y_j \tag{2.42}$$

The upwind indices r and q appearing in Eqn. (2.41) and (2.42) are determined as follows:

$$r=\begin{cases}0 & \langle V_p\rangle_{s_{j+\frac{1}{2}}}\geq 0\\ 1 & \langle V_p\rangle_{s_{j+\frac{1}{2}}}\leq 0\end{cases}\quad and\quad q=\begin{cases}-1 & \langle V_p\rangle_{s_{j-\frac{1}{2}}}\geq 0\\ 0 & \langle V_p\rangle_{s_{j-\frac{1}{2}}}\leq 0\end{cases}$$

The following is the flowchart of the solution algorithm for this set of equations:

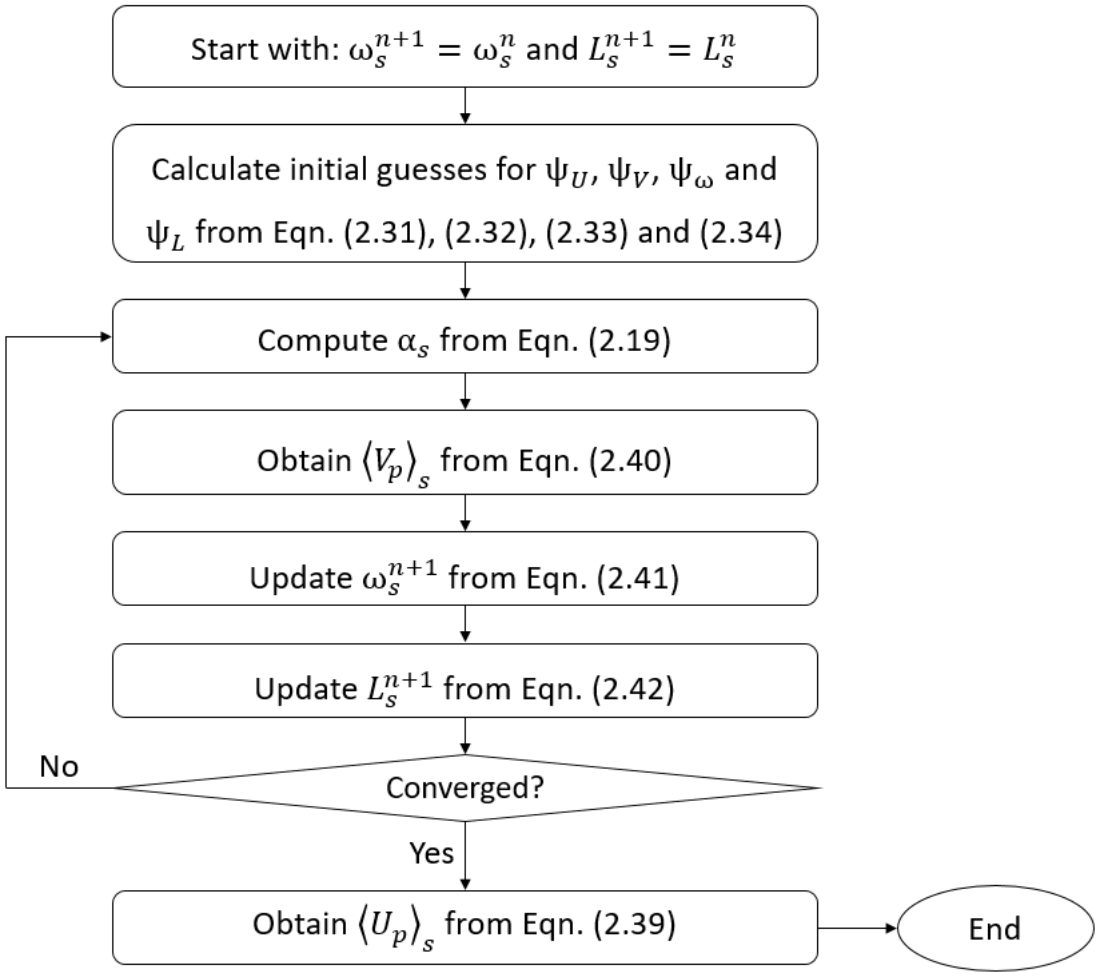

Fig. 2.6: Iteration procedure for cross-stream 1D equations

2.5 Recommendations

When using the DQMOM, a primary source of numerical instability is associated with the solution of Eqn. (2.17), which is very prone to become ill-conditioned. This problem occurs when the

quadrature abscissas of the PSD get very proximal to each other, causing the determinant of the corresponding matrix of coefficients to approach zero. The issue can be mitigated by taking into account the following recommendations:

- As the number of quadrature nodes N increases, the distance between the quadrature abscissas decreases (see Fig. 2.7 as an example), which denotes that the matrix of coefficients will become more ill-conditioned since its columns get closer to each other. In practice, it is usually suggested to select less than 5 nodes.

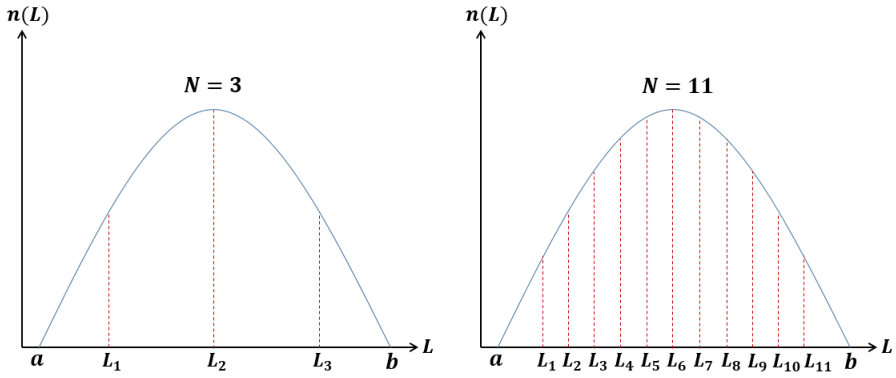

Fig. 2.7: Distance between quadrature abscissas for two different number of nodes

- The nucleation range has to be wide enough to make sure that the corresponding quadrature abscissas are sufficiently distant from each other, and thus to avoid ill-conditioning of the matrix of coefficients (see Fig. 2.8 as an example).

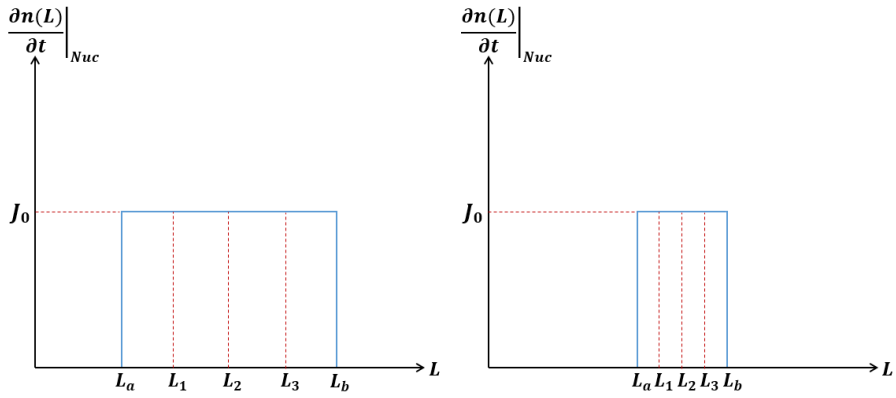

Fig. 2.8: Distance between quadrature abscissas for two different nucleation size range

Chapter 3

Asphaltenes Deposition in Oil Wells

The quasi-1D multi-phase-flow tool, developed for particle-laden channel flows in the previous chapters, will now be employed to study the deposition of asphaltenes in oil wells, as one of the most critical flow assurance problems in petroleum industries. To begin with, a general introduction to asphaltenes will be presented, followed by the corresponding modelling aspects such as the closure relations for the population balance equation, the boundary conditions and so on. Finally, a simulation will be conducted according to a benchmark case, and the results will be compared. will be discussed a concise review of the relevant studies in this area, plus how this work will contribute to the knowledge in this field.

3.1 Introduction to Asphaltenes

In this section, a number of available definitions for asphaltenes will be provided, the factors triggering its precipitation out of crude oil will be discussed, and the corresponding transport processes occurring from precipitation until depositing on the wall will be explained.

3.1.1 Definition of Asphaltenes

The term *asphaltenes* was first introduced in 1837 by the French chemist J.B. Boussingault who defined it as the residue of the distillation of bitumen: insoluble in alcohol and soluble in turpentine. Asphaltenes are the most polar and aromatic fraction of the crude oil heavy components, whose presence results in a significant increase in the oil density and viscosity.

A common method for characterizing the composition of crude oils uses stability criteria to separate the crude oil into four fractions: *Saturates*, *Aromatics*, *Resins* and *Asphaltenes*. Saturates are non-polar molecules which consist of normal-, iso- and cyclo-alkanes, while aromatics are composed of double-bonded hydrocarbon rings similar to benzene. Resins and asphaltenes form a continuum of molecules with increasing weight, aromaticity and hetero-atom (nitrogen, sulfur,...) content. The most commonly accepted definition of the asphaltene fraction is that asphaltenes are soluble in toluene (C_7H_8) and insoluble in normal heptane (C_7H_{16}). However, some other definitions also exist, for instance, by using other normal alkanes as the insoluble delimiter of the asphaltene fraction.

Crude oil is a mixture of a very large number of chemical components. As a consequence of the solubility-based definition, the asphaltene fraction may therefore not be explicitly described by a tractable number of compounds. Asphaltenes are chemically ill-defined and, by definition, poly-disperse. Nevertheless, it is generally agreed that most asphaltene molecules share some common features. They all have a backbone formed from one or more poly-aromatic hydrocarbon cores,

surrounded by peripheral side chains with some hetero-atoms attached. The common types of such hetero-atoms are nitrogen, sulfur and oxygen, as well as several metalic atoms such as vanadium, nickel and iron (see Schutte, 2016). Fig. 3.1 illustrates three of many possible asphaltene molecular structures.

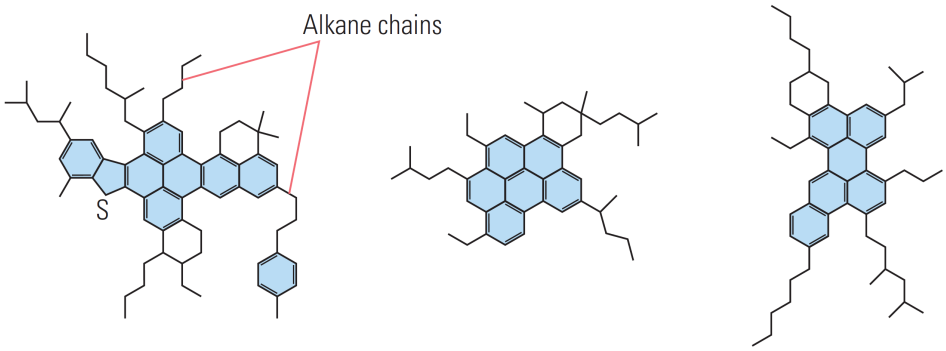

Fig. 3.1: Three possible asphaltene molecular structures (Akbarzadeh et al., 2007)

3.1.2 Stability of Aphaltenes-Crude Oil Dispersion

The stability of a crude oil/asphaltene dispersion is controlled by various factors such as the asphaltene content, the overall oil composition, the pressure and, to a lesser extent, the tenperature. A change in any of these factors might destabilize this dispersion and cause the asphaltenes to precipitate out of the crude oil in either solid or liquid-like form; for convenience and short-hand notation, both are referred to as particles from here on.

In this work, it is assumed that the temperature is homogeneously distributed along the well bore, and also the oil composition stays permanently unaltered. Therefore, pressure is the only remaining element that can trigger the asphaltens to precipitate. Fig. 3.2 exhibits an example of how the asphaltenes solubility in crude oil varies with pressure for two different temperatures (solubility curve).

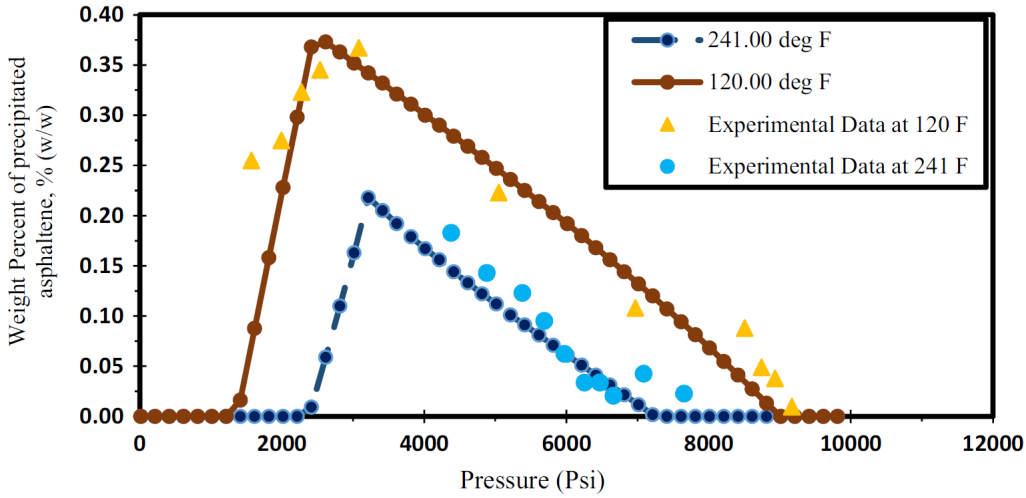

Fig. 3.2: Asphaltene solubility curve (Kor; R. Kharrat; Ayoubi, 2017)

It is seen that at any given temperature, there exists a pressure window, over which the precipitation can take place. The upper and lower ends of the window are refered to as the asphaltene upper onset pressure (AUOP) and lower onset pressure (ALOP), respectively. Moving along the well bore from the bottom hole up to the surface, the pressure decreases, and once the AUOP is reached, the asphaltene particles start nucleating out of the crude oil. This phenomenon continues until the saturation pressure (SATP) (the pressure associated with the peak of the solubility curve), after which the precipitated asphaltenes begin to get dissolved in the oil again.

3.1.3 From Precipitation to Deposit Formation

The formation of the asphaltene deposit layer on the inner surface of the well bore commences with the nucleation of the primary asphaltene particles and ends when the asphaltene aggregates reach and adhere to the wall. In the meantime, the particles can undergo different processes. For example, they can grow as a result of further condensation on their surface, or they may collide and get bonded, resulting in the formation of larger agglomerates. Moreover, non-uniformity of the forces acting on the agglomerates can again break them up into smaller ones. It should be noted that the type of interaction between the agglomerates and the wall determines whether they will stick to or re-entrain from the wall at the instant of touching it.

Apart from the interaction forces between the individual particles and those between the particles and the wall, the flow of the continuous medium (here crude oil) also significantly contributes to the transport and behavior of the asphaltene disperse phase. Therefore, it can be generally said that the competition between the forces induced by the flow on the asphaltene phase and the aforementioned particle-particle/particle-wall interaction forces determines the rates at which the agglomeration, breakup, deposition and re-entrainment processes occur.

Figure below sketches the evolution of the asphaltene particles from the phase separation stage until depositing on the wall, which reduces the diameter of the well bore and thus restricts the oil flow rate.

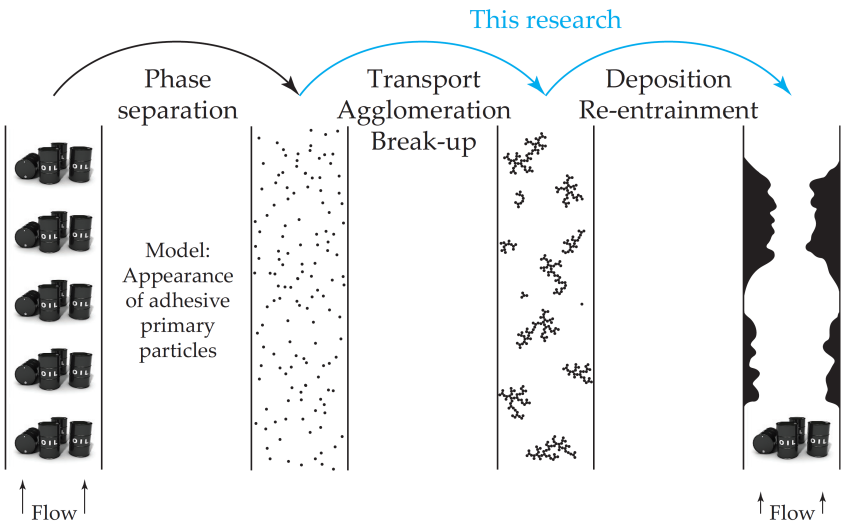

Fig. 3.3: Asphaltene precipitation windlow (Schutte, 2016)

As indicated by the blue arrows, the thermodynamic modelling of the phase separation the asphaltenes is beyond the scope of this work, which will focuse more on the transport and deposition processes.

3.2 Well Bore Geometry Simplification

After being produced from the reservoir, the crude oil comes to the surface through a vertical pipe, whose geometry in this work is simplified using a vertical channel, as illustrated in the following figure:

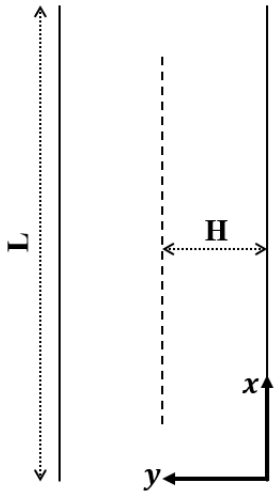

Fig. 3.4: Well bore geometry simplification

Note that all the equations worked out in the previous chapters can be applied to this geometry as well.

3.3 Closure Models for Population Balance Equation

As explained in chapter 2, the spatial and temporal evolution of any population of particles undergoing nucleation, aggregation and breakage processes, as applies to asphaltenes, is described by the population balance equation (PBE). The different parameters appearing in this equation such as collision kernel, breakup kernel etc. need to be closed using proper models that take into account the physics of the phenomenon under investigation. The closure models used in this study are presented in the following subsections.

3.3.1 Nuclearion Size Range

Remember that the nucleation should be considered to occur over a size range (L_a,L_b), rather than a single size, so as to avoid the numerical instability issues associated with the DQMOM. Mansur et al., 2012 found that the asphaltene particles start precipitating out of the crude oil when reaching the size of roughly $1\,\mu\mathrm{m}$. Therefore, the nucleation in this work is presumed to take place within the range ($0.5\,\mu\mathrm{m}$,$1\,\mu\mathrm{m}$).

3.3.2 Nucleation Rate

The nucleation rate of the primary asphaltene particles can be determined using the asphaltene solubility curve (Fig. 3.2), which is characterized by two roughly linear parts inside the precipitation window. This work only focuses on a section of the well bore with a pressure distribution that falls between the AUOP and the pressure associated with the peak of the solubility curve. In this region, the weight percent of the precipitated asphaltene dW would be proportional to the pressure drop dP:

$$dW = C dP \tag{3.1}$$

where $C = 7.7958 \times 10^{-11} (\frac{kg_a}{kg_o.Pa})$ is the slope of the solubility line (note that the subscripts a and o in the unit of C refer to asphaltene and oil, respectively). Therefore, the precipitation rate can be expressed as:

$$\frac{dW}{dt} = C \frac{dP}{dt} \tag{3.2}$$

which, by applying the chain rule, reads:

$$\frac{dW}{dt} = C \frac{dP}{dx} \frac{dx}{dt} = C \frac{dP}{dx} U \tag{3.3}$$

where U is the mean flow velocity in the stream-wise direction. In a vertical well bore, the hydrostatic pressure drop is dominant, so that the pressure gradient can be written as:

$$\frac{dP}{dx} = \rho_c g \tag{3.4}$$

with ρ_c standing for the density of the continuous phase (oil), and g representing the gravitational acceleration. Substituting this in Eqn. (3.3) gives:

$$\frac{dW}{dt} = C \rho_c g U \tag{3.5}$$

The unit of this precipitation rate is $(\frac{kg_a}{kg_o.s})$, which should be converted to $(\frac{number}{m_o^3.s})$ to be consistent with the unit of the nucleation rate J_0, appearing in the PBE, as follows:

$$J_0 = \frac{\rho_c}{\rho_p} \frac{1}{V_p} \frac{dW}{dt} = \frac{C \rho_c^2 g U}{\rho_p V_p} \tag{3.6}$$

where ρ_p is the asphaltene density, and V_p represents the average volume of nucleating particles, given by:

$$V_p = \frac{\pi}{6} L_p^3 = \frac{\pi}{6} \left(\frac{L_a + L_b}{2} \right)^3 \tag{3.7}$$

3.3.3 Collision Kernel

Saffman et al., 1956 came up with an expression for the collision kernel due to fluid shear for particles smaller than the Kolmogorov length scale in turbulent flows:

$$\beta(L,\lambda) = \frac{1}{8}\sqrt{\frac{8\pi}{15}}\sqrt{\frac{\varepsilon}{\nu}}(L+\lambda)^3 \tag{3.8}$$

where ε is the dissipation rate of the turbulent kinetic energy, ν is the fluid dynamic viscosity, and the terms inside the brackets are the sizes of the particles to collide. In this work, the binary collision assumption is made, according to which every collision occurs between not more than two particles.

3.3.4 Collision Efficiency

In order to form an agglomerate, the two colliding particles should get bonded and adhere to each other when touching. The probability of this to occur is referred to as the collision efficiency E. No proper collision efficiency model for asphaltenes was found in the literature. Therefore, it was decided to improvise a model based on the expectation that the larger the diameter of the colliding particles, the lower the collision efficiency due to less contact time at the instant of collision. Alopaeus et al., 1999 have proposed a model for the collision efficiency between two liquid droplets, which has the following functionality of the droplets diameter (L, λ):

$$E(L,\lambda) = exp\left[-\left(\frac{L\lambda}{L+\lambda}\right)^4\right] \tag{3.9}$$

Even though the collision physics associated with the asphaltenes and droplets might be different, the same functionality is employed in this work, except that two additional constants C_1 and C_2 are incorporated for tuning purposes as follows:

$$E(L,\lambda) = C_1 exp\left[-C_2\left(\frac{L\lambda}{L+\lambda}\right)^4\right] \tag{3.10}$$

3.3.5 Breakup Kernel

The breakup of agglomerates is caused by stresses that are induced as a result of the spatial variations of hydrodynamic forces. Therefore, modelling the agglomerate fragmentation process is much more complex than predicting how frequent the agglomerates collide with each other. Closure relations for the breakup kernel are typically empirical, which relate the breakup rate to the particle diameter and the shear stress in the fluid. Barthelmes et al., 2003 proposed the expression below for the breakup rate of agglomerates with fractal structure:

$$a(L) = \varrho G^{\upsilon} V_p^{\frac{1}{3}} \left(\frac{L}{L_p}\right)^{\frac{3}{D_f}} \tag{3.11}$$

where G is the average fluid shear rate ($G = \sqrt{\frac{\varepsilon}{\nu}}$ in a turbulent flow), D_f agglomerate fractal dimension, ϱ a proportionality constant, and υ (not to be confused with ν) a constant related to the

aggregate strength. Choosing the values $\varrho = 3.88\times10^{-3}$ and $\upsilon = 2$, as used by Faraji et al., 2010, and assuming that the particles are spherical ($D_f = 3$), Eqn. (3.11) takes the following form:

$$a(L) = 2.808\times10^{-3} G^2 L \tag{3.12}$$

3.3.6 Daughter Distribution Function

The expression below has been suggested by Marchisio et al., 2003 for the daughter distribution function:

$$b^k(\lambda) = \lambda^k \frac{m^{k/3} + n^{k/3}}{(m+n)^{k/3}} \tag{3.13}$$

which, assuming symmetric binary fragmentation (m=1 & n=1), turns into:

$$b^k(\lambda) = \lambda^k \, 2^{1-\frac{k}{3}} \tag{3.14}$$

3.4 Boundary Conditions

3.4.1 Stream-Wise 1D Equations

Neglecting the pressure variations at the bottom (inlet) and top (outlet) of the well bore section under study, one may write:

$$\langle \overline{P}_c \rangle \Big|_{Inlet} = P_I \quad , \quad \langle \overline{P}_c \rangle \Big|_{Outlet} = P_O$$

which translate into zero Dirichlet boundary conditions for Eqn. (1.29):

$$\langle \overline{P}_c \rangle' \Big|_{Inlet} = 0 \quad , \quad \langle \overline{P}_c \rangle' \Big|_{Outlet} = 0$$

The boundary conditions for Eqn. (1.28) can be adopted from Eqn. (1.15):

$$\frac{\partial(H\langle \overline{U}_c \rangle)}{\partial x}\Big|_{Inlet} = 0 \quad , \quad \frac{\partial(H\langle \overline{U}_c \rangle)}{\partial x}\Big|_{Outlet} = 0$$

Assuming zero particle flux at the inlet leads to the following boundary conditions for

Eqn. (2.35):

$$\alpha_s \langle \overline{U}_p \rangle_s \Big|_{Inlet} = 0$$

Eqn. (2.36):

$$\alpha_s \langle \overline{V}_p \rangle_s \Big|_{Inlet} = 0$$

Eqn. (2.37):

$$\omega_s|_{Inlet} = 0$$

Eqn. (2.38):

$$\omega_s L_s|_{Inlet} = 0$$

Furthermore, zero derivative of the mean particle-phase velocities are imposed at the outlet as the boundary conditions for Eqn. (2.39) and (2.40):

$$\left.\frac{\partial \langle \overline{U}_p \rangle_s}{\partial x}\right|_{Outlet} = 0 \quad , \quad \left.\frac{\partial \langle \overline{V}_p \rangle_s}{\partial x}\right|_{Outlet} = 0$$

3.4.2 Cross-Stream 1D Equations

The symmetry condition applies to all the cross-stream 1D equations as follows:

$$\left.\frac{\partial(\cdots)}{\partial y}\right|_{y=H} = 0$$

where $(\cdots)$ refers to any fluid or particulate phase variable, excluding the cross-stream mean particle velocity, which will be zero along the centerline of the channel:

$$\langle V_p \rangle_s|_{y=H} = 0$$

The same near-wall boundary conditions as used for the turbulent kinetic energy, turbulent dissipation rate, and cross-stream 1D RANS equations in Chapter 1, are applied here as well. Close to the wall, the turbulent fluctuations vary drastically, which will highly affect the velocity field of the particulate phase. However, because of using wall function in this work, no information is available on the profiles of the turbulent kinetic energy and its dissipation rate between the logarithmic layer and the wall. Therefore, the particle-phase momentum equations cannot be solved in this region. A possible solution to this issue is to specify the boundary conditions of these equations at the center the wall-function grid cell (Fig. 3.5) rather than at the wall, which requires estimation of the mean particle velocity components at this position. In fact, this allows to sort of skip the region between the logarithmic layer and the wall.

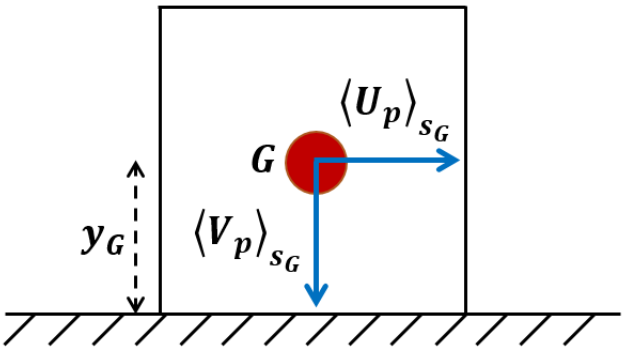

Fig. 3.5: Mean velocity components of a particle when it arrives at the wall-function grid point

Supposing that the particles act as perfect tracers when arriving at $y = y_G$, their stream-wise mean velocity would be equal to that of the fluid:

$$\langle U_p \rangle_{s_G} = \langle U_c \rangle_G$$

which will serve as the boundary condition for Eqn. (2.39). In the cross-stream direction, no mean flow velocity exists, so that the particles move mainly under the influence of the turbulent fluctuations. According to Eskin et al., 2011, the most probable fluctuating velocity of the particles towards the wall at $y = y_G$ can be approximated by:

$$\langle V_p \rangle_{s_G} = \sqrt{\frac{\langle V_c' V_c' \rangle_G}{2\pi}} \tag{3.15}$$

where $\langle V_c' V_c' \rangle_G$ is the root-mean-square cross-stream fluid fluctuating velocity at the wall-function grid point. This will provide the boundary condition for Eqn. (2.40).

Apart from the discussion above, the velocity of the particles at the position of the wall is still needed to update the wall fluxes appearing in the stream-wise 1D equations (the terms with the subscript $_0$). In this work, it is presumed that any particle only has a cross-stream velocity component at the moment of touching the wall (Fig. 3.6).

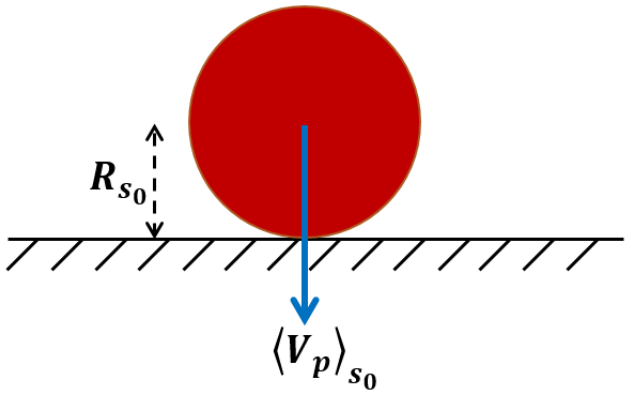

Fig. 3.6: Cross-stream mean velocity of a particle at the moment of touching the wall

This velocity, also referred to as the deposition velocity, can be estimated from:

$$\langle V_p \rangle_{s_0} = \sqrt{\frac{\langle V_c' V_c' \rangle_0}{2\pi}} \tag{3.16}$$

where $\langle V_c' V_c' \rangle_0$ is the root-mean-square cross-stream fluid fluctuating velocity at the particle center, which can be obtained from the empirical model proposed by Guha, 2008:

$$\sqrt{\langle V_c' V_c' \rangle_0} = \frac{5 \times 10^{-3} (\delta_s^+)^2}{1 + 2.923 \times 10^{-3} (\delta_s^+)^{2.128}} u_* \qquad 0 < \delta_s^+ < 200 \tag{3.17}$$

where δ_s^+ is the dimensionless distance of the particle center from the wall:

$$\delta_s^+ = \frac{R_{s_0} u_*}{\nu}$$

Based on this model, larger particles will experience greater turbulent fluctuations and thus will have higher deposition velocity.

3.5 Deposition Flux

When studying the transport of asphaltene particles in oil wells, it is of high importance to determine the deposition flux at the wall of the well bore, which reveals how the deposit layer thickness will grow along the well bore and also in time. In the DQMOM, the deposition flux for each particle class is computed from:

$$Q_s = \Phi \frac{\pi}{6} \Big(L_s^3 \, \omega_s \langle V_p \rangle_s \Big)_0 \tag{3.18}$$

where L_s, ω_s and $\langle V_p \rangle_s$ are the characteristic length, number density and deposition velocity of the particle class, respectively. The symbol Ψ is called the deposition efficiency and is taken equal to unity in case of a fully absorbing wall. The total deposition flux results from the summation over the contributions from all the particle classes:

$$Q = \Phi \frac{\pi}{6} \sum_{s=1}^{N} \Big(L_s^3 \, \omega_s \langle V_p \rangle_s \Big)_0 \tag{3.19}$$

3.6 Results and Discussion

A general quasi-1D model was developed for internal particle-laden flows in the previous chapters, by one-way coupling of a single-phase flow model, the Eulerian-Eulerian model and the population balance equation. In this chapter, the closure expressions, boundary conditions, simplifications etc., required for modelling the problem of asphaltenes transport and deposition in oil wells, were provided. Now, a simulation test case will be set up according a benchmark case, and the corresponding results will be presented and compared.

3.6.1 Test Case Setup

The work of Kurup et al., 2011 is considered as the benchmark case, according to which the simulation test case will be set up. They developed a simulator to predict the thickness profile of the asphaltene deposit layer in oil well bores, which consists of a thermodynamic module and a deposition module. The thermodynamic module uses the PC-SAFT equation of state to determine the asphaltene precipitation rate, which then serves as input to the deposition module to obtain the magnitude of the deposition flux along the well bore. This simulator was employed to study the deposition in the Kuwait's Marrat well bore, for which the measurements of the deposition profile have been reported in the literature. The well bore operating conditions and parameters and the corresponding fluid data can be found in the following table:

Well bore depth (ft)	15000
Tube diameter (in)	2.75
Flow rate $(^{STB}/_{Day})$	5000
Oil density $(^{kg}/_{m^3})$	850
Oil viscosity (cp)	3.95

Table 3.1: Well bore operating conditions and parameters

In addition, Fig. 3.7 shows the phase behavior of the Kuwait's Marrat oil in terms of asphaltene precipitation, where the oblique grey solid line represents the oil path going through the UAOP (red circle), SATP (blue square) and LAOP (green triangle). It is seen that the temperature also varies along the well bore.

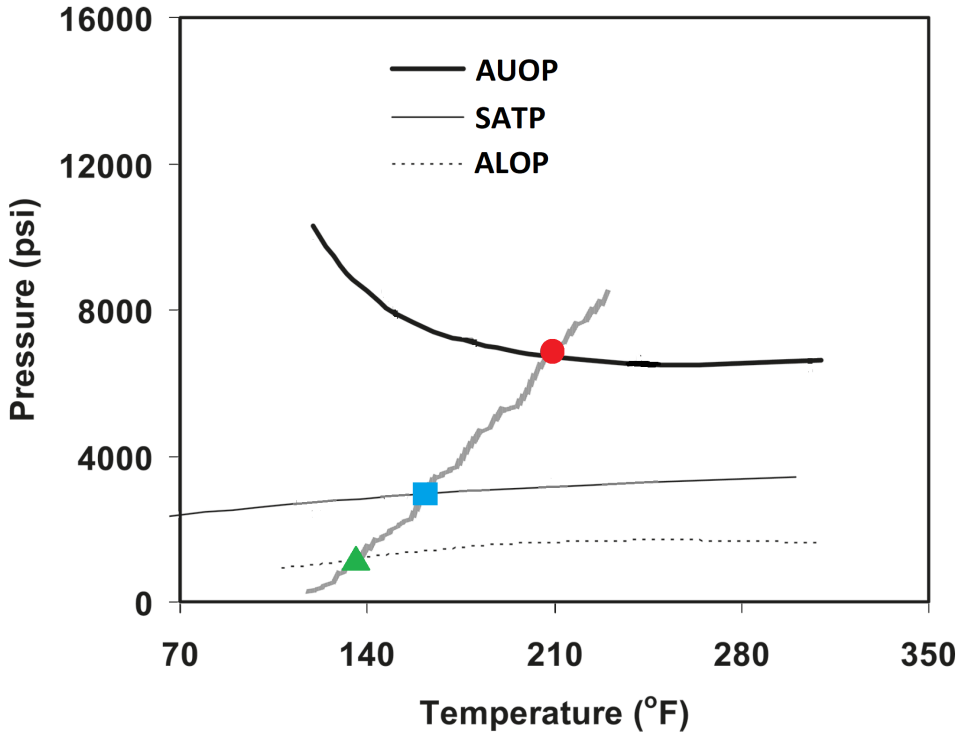

Fig. 3.7: Phase behavior of Kuwait's Marrat oil in terms of asphaltene precipitation

In this study, the following simplifications are made:

- The focus is only put on a section of the well bore where the precipitation is taking place (the region between the AUOP and SATP). According to Fig. (3.7), the UAOP and SATP are equal to 3000 psi and 7000 psi, which approximately translate into the depths of 8000 ft and 19000 ft, respectively, considering only the hydrostatic pressure drop and assuming that the well bore opens up to the atmospheric pressure at the surface. This means that the precipitation is ongoing from the bottom hole at 15000 ft up to the depth of 8000 ft.
- As explained in section 3.3.2, the temperature is assumed to be uniform along the well bore, leading to a roughly constant asphltene precipitation rate, which can be calculated using Eqn. (3.6) to be 8.44×10^{12} $(\frac{number}{m_o^3.s})$. Note that the asphaltene density has been taken equal to that of the oil.

For the simulation test case, the length of the well-bore section under study is considered to be 7000 ft, with the bottom and top located at the depths of 15000 ft and 8000 ft, respectively. The number of grid cells in the stream-wise (N_x) and cross-stream (N_y) directions are set 75 and 10. The pseudo time step size is chosen 0.005 s, and the steady-state convergence criterion is set to be 10^{-12}.

3.6.2 Test Case Results

The following figure shows the thickness profile of the asphaltene deposit layer, obtained in this study using the quasi-1D model, after two months of oil production along with the one reported by Kurup et al., 2011 and a measured well data:

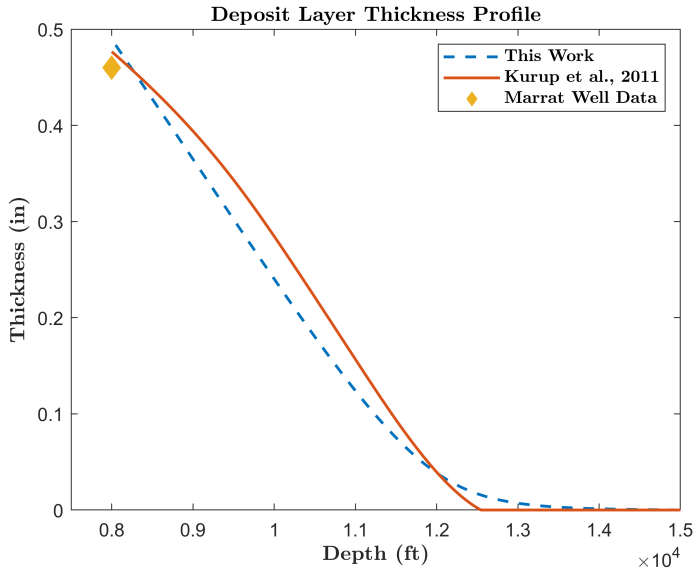

Fig. 3.8: Comparison between the thickness profiles of the deposit layer, associated with this work and Kurup et al., 2011, after two months of oil production, plus a measured well data

As it is seen, the results generally match each other but are still slightly different. This is essentially due to the fact that the temperature variation, causing the precipitation rate to change along the well bore, has not been taken into account in this study, as apposed to the work of Kurup et al., 2011. It should be noted that this match was obtained by tuning the constants C_1 and C_2, appearing in the collision efficiency model, to be 8.5×10^{-2} and 4×10^{22}, respectively. The simulation was repeated for the double and half of these values as well, to investigate how the deposition profile will vary with respect to these constants. The corresponding results have been exhibited in the following figures:

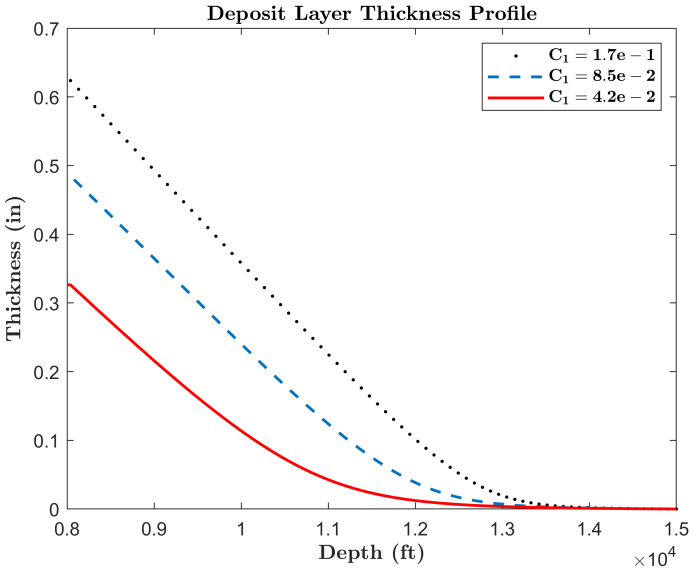

Fig. 3.9: Sensitivity analysis with respect to C_1

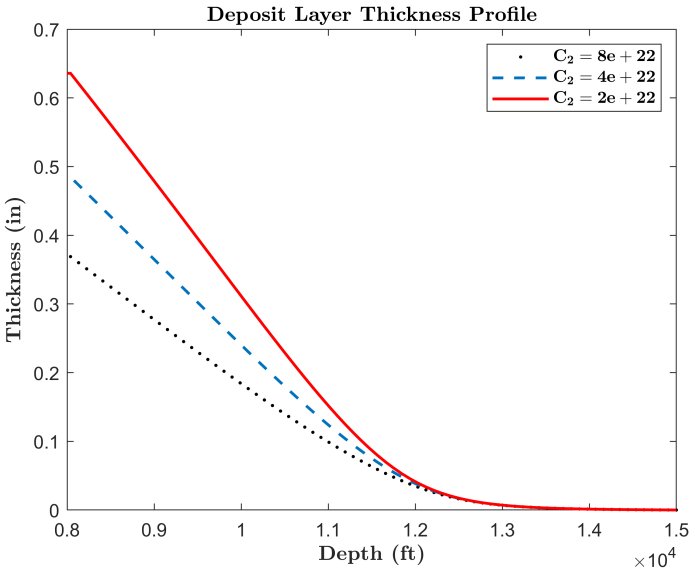

Fig. 3.10: Sensitivity analysis with respect to C_2

which suggest that the collision efficiency plays a prominent role in determination of the asphaltene deposition profile and needs to be modeled properly. In order to make an interpretation of these graphs, it is necessary to take a look at Fig. 3.11 and 3.12, which describe the collision efficiency as a function of the particle diameter for the same values of C_1 and C_2 as used above:

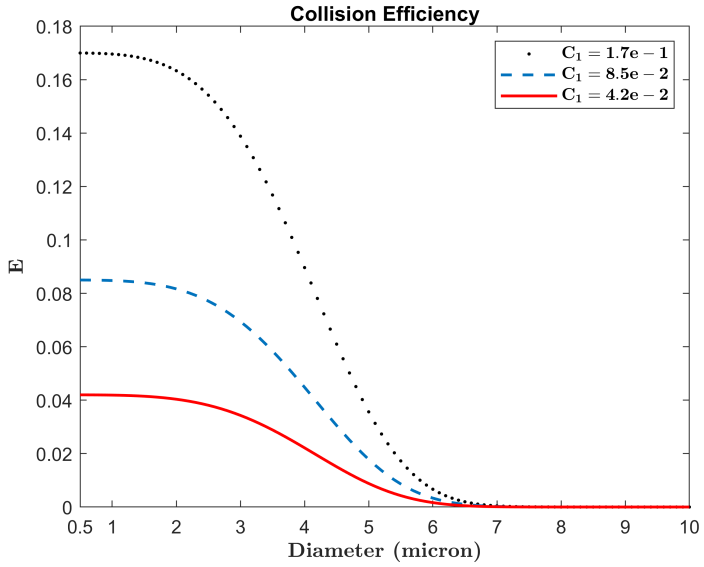

Fig. 3.11: The effect of change in C_1 on the collision efficiency

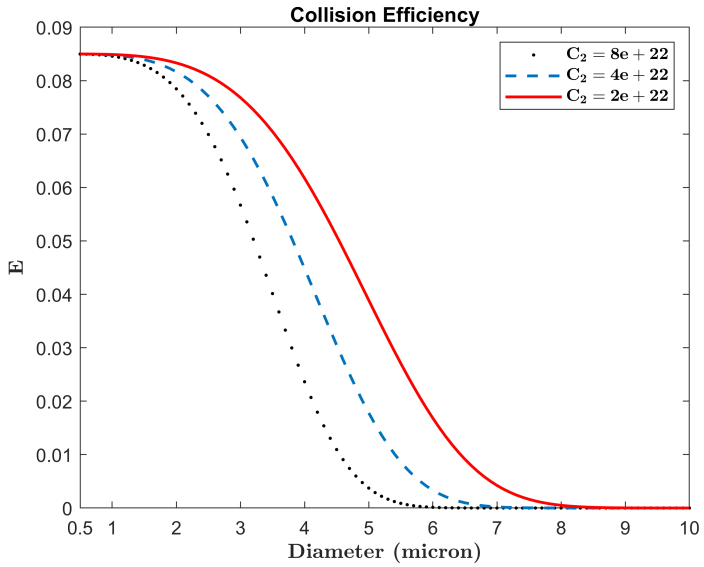

Fig. 3.12: The effect of change in C_2 on the collision efficiency

One can clearly see that decreasing C_1 or increasing C_2 leads to the reduction of the collision efficiency, in which case the aggregation process will occur less frequently, and the average particle size will decrease. As also mentioned before, the smaller particles tend to have lower deposition velocity, which in turn results in the less growth of the deposit layer thickness over a given period of time.

3.7 Conclusions

The quasi-1D multi-phase-flow model was used to study the problem of asphaltenes deposition in oil wells. A simulation test case was set up according to the work of Kurup et al., 2011, and the corresponding results were presented and compared, based on which the following conclusions can be made:

- The deposition profile predicted by the quasi-1D model was generally in line with the one reported by Kurup et al., 2011.
- The results of the sensitivity analysis with respect to the collision efficiency revealed that this parameter plays an important role in determining of the deposition profile and needs to be modeled accurately.

3.8 Recommendations

The recommendations below should be considered to improve the capability of the quasi-1D model in predicting the asphaltenes deposition profile in oil wells:

- It is of high importance to accurately account for the effects of the pressure and temperature variations along the well bore on the phase behavior of the crude oil and thus the asphaltenes precipitation rate, by coupling the quasi-1D model with an appropriate thermodynamic model.
- The collision efficiency of the asphaltenes should be modeled properly, by taking into account the physics involved in the collision of the corresponding particles.
- It is also desirable to develop a wall function for describing the near-wall velocity field of the particles, which can serve as the boundary condition for the particle-phase momentum equations.

Bibliography

AKBARZADEH, Kamran et al., 2007. Asphaltenes-problematic but rich in potential. *Oilfield Review*. Vol. 19, no. 2, pp. 22–43.

ALOPAEUS, Ville; KOSKINEN, Jukka; KESKINEN, Kari I, 1999. Simulation of the population balances for liquid–liquid systems in a nonideal stirred tank. Part 1 Description and qualitative validation of the model. *Chemical Engineering Science*. Vol. 54, no. 24, pp. 5887–5899.

ANDERSON, John David; WENDT, J, 1995. *Computational fluid dynamics*. Springer.

APSLEY, David, 2007. CFD calculation of turbulent flow with arbitrary wall roughness. *Flow, Turbulence and combustion*. Vol. 78, no. 2, pp. 153–175.

BARTHELMES, Georg; PRATSINIS, Sotiris E; BUGGISCH, Hans, 2003. Particle size distributions and viscosity of suspensions undergoing shear-induced coagulation and fragmentation. *Chemical Engineering Science*. Vol. 58, no. 13, pp. 2893–2902.

ESKIN, D; RATULOWSKI, J; AKBARZADEH, K; PAN, S, 2011. Modelling asphaltene deposition in turbulent pipeline flows. *The Canadian Journal of Chemical Engineering*. Vol. 89, no. 3, pp. 421–441.

FARAJI, Marjan; SOLAIMANY NAZAR, Ali R, 2010. A Study of the Dynamic Evolution of Asphaltene Aggregate Size Distribution Using Monte Carlo Simulation. *Energy & Fuels*. Vol. 24, no. 9, pp. 4952–4960.

GUHA, Abhijit, 2008. Transport and deposition of particles in turbulent and laminar flow. *Annu. Rev. Fluid Mech.* Vol. 40, pp. 311–341.

HEINZ, S, 2003. *Statistical Mechanics of Turbulent Flows*. Springer-Verlag, Berlin.

JOHN, V; ANGELOV, I; ÖNCÜL, AA; THÉVENIN, D, 2007. Techniques for the reconstruction of a distribution from a finite number of its moments. *Chemical Engineering Science*. Vol. 62, no. 11, pp. 2890–2904.

KOR, Peyman; KHARRAT, Riyaz, 2016. Prediction of the asphaltene deposition profile along a wellbore during natural production from a reservoir. *Energy Sources, Part A: Recovery, Utilization, and Environmental Effects*. Vol. 38, no. 19, pp. 2837–2844.

KOR, Peyman; KHARRAT, Riyaz; AYOUBI, Abdoljalal, 2017. Comparison and evaluation of several models in prediction of asphaltene deposition profile along an oil well: a case study. *Journal of Petroleum Exploration and Production Technology*. Vol. 7, no. 2, pp. 497–510.

KURUP, Anjushri S; VARGAS, Francisco M; WANG, Jianxin; BUCKLEY, Jill; CREEK, Jefferson L; SUBRAMANI Hariprasad, J; CHAPMAN, Walter G, 2011. Development and application of an asphaltene deposition tool (ADEPT) for well bores. *Energy & Fuels*. Vol. 25, no. 10, pp. 4506–4516.

MANSUR, Claudia RE; MELO, Andressa R de; LUCAS, Elizabete F, 2012. Determination of asphaltene particle size: influence of flocculant, additive, and temperature. *Energy & Fuels*. Vol. 26, no. 8, pp. 4988–4994.

MARCHISIO, Daniele L; FOX, Rodney O, 2005. Solution of population balance equations using the direct quadrature method of moments. *Journal of Aerosol Science*. Vol. 36, no. 1, pp. 43–73.

MARCHISIO, Daniele L; FOX, Rodney O, 2007. *Multiphase reacting flows: modelling and simulation*. Springer.

MUKHTAR, Safyan; ILTAF HUSSAIN, Arshed Ali, 2012. Quadrature method of moments for solving volume-based population balance models. In: *Quadrature method of moments for solving volume-based population balance models*. *World Applied Sci. J*.

NIEUWSTADT, Frans TM; WESTERWEEL, Jerry; BOERSMA, Bendiks J, 2016. *Turbulence: introduction to theory and applications of turbulent flows*. Springer.

RAMIREZ-JARAMILLO, E; LIRA-GALEANA, C; MANERO, O, 2006. Modeling asphaltene deposition in production pipelines. *Energy & fuels*. Vol. 20, no. 3, pp. 1184–1196.

SAFFMAN, PGF; TURNER, JS, 1956. On the collision of drops in turbulent clouds. *Journal of Fluid Mechanics*. Vol. 1, no. 1, pp. 16–30.

SCHÄFER, Michael, 2006. *Computational engineering: Introduction to numerical methods* . Springer.

SCHUTTE, KCJ, 2016. *A hydrodynamic perspective on the formation of asphaltene deposits*. PhD thesis. Delft University of Technology.

SCHWARZKOPF, John D; SOMMERFELD, Martin; CROWE, Clayton T; TSUJI, Yutaka, 2011. *Multiphase flows with droplets and particles*. CRC press.

VARGAS, Francisco M; CREEK, Jeff L; CHAPMAN, Walter G, 2010. On the development of an asphaltene deposition simulator. *Energy & Fuels*. Vol. 24, no. 4, pp. 2294–2299.

Appendix

Thomas algorithm is used to solve the matrix form of a system of algebraic equations and is in fact a simplified version of the Gaussian Elimination method, which is applicable when the corresponding matrix of coefficients is tri-diagonal. This algorithm has been explained below for a 5×5 matrix equation as an example:

$$\begin{bmatrix} b_1 & c_1 & 0 & 0 & 0 \\ a_2 & b_2 & c_2 & 0 & 0 \\ 0 & a_3 & b_3 & c_3 & 0 \\ 0 & 0 & a_4 & b_4 & c_4 \\ 0 & 0 & 0 & a_5 & b_5 \end{bmatrix} \times \begin{bmatrix} x_1 \\ x_2 \\ x_3 \\ x_4 \\ x_5 \end{bmatrix} = \begin{bmatrix} d_1 \\ d_2 \\ d_3 \\ d_4 \\ d_5 \end{bmatrix}$$

- Step1:

$$W_1 = \frac{c_1}{b_1} \qquad G_1 = \frac{d_1}{b_1}$$

- Step2:

$$W_i = \frac{c_i}{b_i - d_i W_{i\text{-}1}} \qquad i = 2, 3, 4, 5$$

- Step3:

$$G_i = \frac{d_i - a_i G_{i\text{-}1}}{b_i - a_i W_{i\text{-}1}} \qquad i = 2, 3, 4, 5$$

- Step4:

$$x_5 = G_5$$

- Step5:

$$x_i = G_i - W_i x_{i+1} \qquad i = 1, 2, 3, 4$$